

Region-of-interest reconstructions from truncated 3D x-ray projections

Robert Azencott¹, Bernhard G. Bodmann¹, Demetrio Labate¹,
Anando Sen², Daniel Vera¹

June 28, 2022

Abstract

This paper introduces a method of region-of-interest (ROI) reconstruction from truncated 3D X-ray projections, consisting of a wavelet-based regularized iterative reconstruction procedure that, under appropriate conditions, converges within the ROI to an exact or highly accurate solution. ROI tomography is motivated by the goal to reduce the overall radiation exposure when primarily the reconstruction of a specified region rather than the entire object is required. Our approach assumes that only the 3D truncated X-ray projections, i.e., the projection data restricted to the image of the ROI, are known and does not assume any previous knowledge about the density function, except for standard assumptions about integrability and regularity needed to ensure that forward and backward transforms are well defined. We provide rigorous theoretical justification for the convergence of our regularized reconstruction algorithm in the continuous setting and prove the existence of a critical radius of a spherical ROI that ensures the convergence of the algorithm. Theoretical results are validated numerically using simulated acquisition and truncation of projection data for various acquisition geometries and ROI sizes and locations. We provide a numerical analysis of the ROI reconstruction stability as a function of the ROI size, showing that our algorithm converges also for ROI sizes which are rather small with respect to

¹Department of Mathematics, University of Houston, Houston, Texas 77204, USA.

²Biomedical Engineering, University of Houston, Houston, Texas 77204, USA.

the support of the density function.

Keywords: computed tomography, interior tomography, region-of-interest tomography, x-ray transform, wavelets.

1 Introduction

Computed Tomography (CT) is a non-invasive scanning procedure that is routinely used in medical diagnostics and interventional medical procedures. By its nature, CT involves patient exposure to X-ray radiation, with health risks of radiation-induced carcinogenesis which are essentially proportional to radiation exposure levels [1, 2]. To reduce radiation exposure in CT, several strategies have been explored such as sparsifying the numbers of X-ray projections or truncating the projections so that only X-rays intersecting a small region-of-interest (ROI) are acquired.

The mathematical problem of reconstructing an image from its projections is an ill-posed problem, meaning that small perturbations in the projections may lead to significant errors in reconstruction. As a result, several approximated or regularized reconstruction formulas have been introduced over the years, such as the classical Filtered Back-Projection or FDK algorithms [3, Ch.5]. Note that these methods are designed to work using complete projected data. When the X-ray projections are truncated, the reconstruction problem becomes severely ill posed [4] and naive numerical reconstruction algorithms (e.g., direct application of a global reconstruction formula, with the missing projection data set to zero) may produce serious instability and visual artifacts.

The problem of ROI reconstruction in CT has been studied in multiple papers and using a variety of methods (see, for example, the recent reviews [5, 6] and the references therein). In particular, recent remarkable results have shown that it is often possible to derive analytic ROI reconstruction formulas from truncated data, if the ROI is chosen with certain restrictions (cf. [7, 8, 9]). Such explicit ROI reconstruction formulas from truncated X-ray data depend on the specific acquisition modalities and usually impose restrictions on ROI geometry so that, for example, some prior knowledge of the density function in the ROI is needed or the ROI cannot lie strictly inside the support of the object. On the other hand, iterative methods provide an

alternative approach for the reconstruction from truncated-data problem and can be applied to essentially any type of acquisition mode (cf. [10, 11]). With respect to analytic formulas, however, these methods are computationally more intensive, especially for 3D data. However, advances in computational capabilities (e.g., [12]) and recent ideas from compressed sensing (e.g., [13]) offer powerful tools to overcome this limitation.

In this paper, we present a new method for accurate 3D ROI reconstruction from truncated X-ray projections, which is *generic* in the sense that it can be implemented for any pair of forward and backward transforms and does not impose restrictions on the geometry or location of the ROI. Our approach is based on the idea of the Iteration Reconstruction-Reprojection (IRR) algorithm [14, 15, 16] and can be briefly summarized as follows. Let X^{-1} be any formula or algorithm which is known to achieve correct reconstruction from a *complete* set of the X-ray projections of an image f . Our approach iteratively uses X^{-1} and a wavelet-based regularization operator to reconstruct the f within the ROI using *only* ROI-focused truncated X-ray data. As an alternative regularization step, we also consider a method that employs a smoothing convolution operator every time we re-project the data, before the reconstruction step.

As a main original contribution, we provide a rigorous mathematical analysis of our regularized iterative algorithm of ROI reconstruction in the continuous setting and prove the *existence of a critical size* of the ROI ensuring the convergence of the algorithm. This critical size does not depend on the location of the ROI within the support of the density function. We also present a practical procedure to determine the minimal radius of spherical ROIs for which the ROI reconstruction algorithm remains accurate and feasible. In order to do that, we link the critical ROI volume to the spectral radius of a specific linear operator. We illustrate our theoretical results by systematic numerical demonstration of the ROI reconstruction quality in 3D from truncated CT projections using simulated X-ray acquisitions. Our numerical results show that the critical radius can be chosen to be rather small with respect to the size of the support of the density function.

The rest of the paper is organized as follows. In Section 2, we recall the definition of the X-ray transform and define its smooth truncated version. In Section 3, we describe an algorithm for the ROI reconstruction from truncated 3D projections which includes a wavelet-based regularization strategy. In Section 4, we discuss the convergence properties of the algo-

rithm and prove a convergence result valid in the continuous setting. In Section 5, we illustrate the application of the ROI reconstruction algorithm from Section 3 using different discrete forward and backward transforms and simulated acquisition, including parallel beam, spiral and circular acquisition. We examine the performance of the algorithm in terms of accuracy and its stability as a function of the size of the ROI. In Section 6, we present an alternative ROI reconstruction framework which uses a different regularization approach based on a smoothing convolution operator and is useful to prove a more general convergence result. Finally, we make some concluding remarks about future work in Section 7.

2 The X-ray transform and its inversion

We start by introducing the mathematical formalism that is needed to present the problem of the reconstruction of a function from its X-ray projections.

2.1 The X-ray transform and the Riemannian manifold of X-rays

X-ray tomography aims to reconstruct the unknown density function f of a 3D object from a set of projections of f obtained by recording radiation attenuation along the rays through the support of f . If f is an integrable function, the *X-ray Transform* of f consists of the line integrals of f over the rays $r(u, \theta)$ passing through $u \in \mathbb{R}^3$ and parallel to the unit vector $\theta \in S^2$:

$$Xf(u, \theta) = \int_{-\infty}^{\infty} f(u + t\theta) dt. \quad (1)$$

Since $Xf(u, \theta)$ does not change if u is moved parallel to θ , it is sufficient to restrict u to the plane through the origin that is orthogonal to θ in \mathbb{R}^3 , henceforth denoted by $T(\theta)$. Thus, Xf is a function on the tangent bundle of the sphere that we denote by $\mathcal{R} = \{(u, \theta) : \theta \in S^2, u \in T(\theta)\}$. Note that the pairs (u, θ) and $(u, -\theta)$ give the same ray $r(u, \theta)$, so that the mapping $(u, \theta) \rightarrow r(u, \theta)$ is a double covering of \mathcal{R} onto a 4-dimensional Riemannian quotient manifold. The associated Riemannian volume element on \mathcal{R} is $du dQ(\theta)$, where $dQ(\theta)$ is the surface area on S^2 and du is the Lebesgue measure on the plane $T(\theta)$.

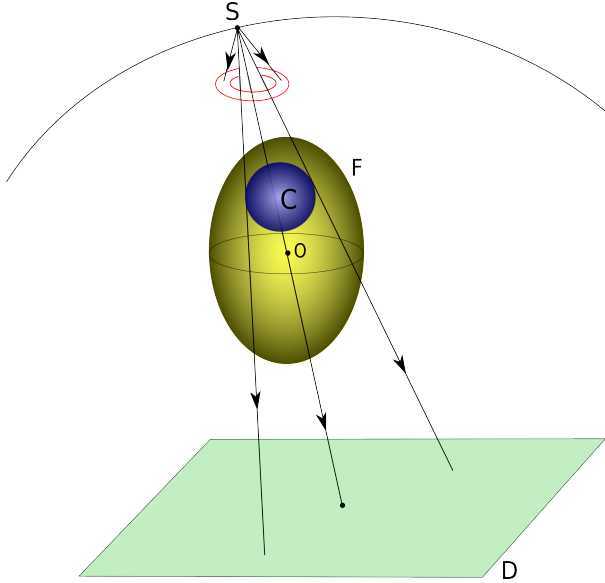


Figure 1: C -truncated X-ray acquisition. The x-ray projections are restricted to the set of rays intersecting the ROI region C .

2.2 ROI-truncated X-ray acquisition

As discussed in the introduction, a natural strategy to reduce radiation exposure consists in restricting X-ray acquisition to the X-rays passing through a small region-of-interest (ROI) contained inside the support of the object with density function f , as illustrated in Figure 1. For simplicity, we assume that the ROI is a ball $C \subset \mathbb{R}^3$ contained inside the support of f and we call *C -truncated X-ray projections* the values of $Xf(u, \theta)$ restricted to those $(u, \theta) \in \mathcal{R}$ for which the rays $r(u, \theta)$ pass through the ball C . We denote the subset of \mathcal{R} corresponding to rays passing through C as

$$\mathcal{R}_C = \{(u, \theta) : r(u, \theta) \cap C \neq \emptyset\}.$$

Correspondingly, we define the *C -truncated X-ray transform* $Y_C f$ of f as the function

$$Y_C f = 1_{\mathcal{R}_C} X f, \quad (2)$$

where 1_S is the indicator function of the set S .

The problem of interest in ROI tomography is to compute an exact or highly accurate reconstruction of f *inside* the ball C or, at least, inside

a slightly smaller ball concentric with C , using only the C -truncated X-ray projections. Note that the truncated transform Y_C introduces abrupt discontinuities in the X-ray projections. Before attempting the ROI reconstruction of f , in the next section we will introduce a smoothed version of $Y_C f$.

2.3 Smoothed truncation of the X-ray projections

We consider the class of functions with compact support inside the open ball $B_\rho \subset \mathbb{R}^3$ of radius ρ centered at the origin. We denote by Ω_ρ the subset of \mathcal{R} associated with the rays passing through B_ρ , that is $\Omega_\rho = \{(u, \theta) \in \mathcal{R} : r(u, \theta) \cap B_\rho \neq \emptyset\}$. Thus, Ω_ρ is an open submanifold of \mathcal{R} with compact closure in \mathcal{R} and the natural Riemannian volume element at $(u, \theta) \in \Omega_\rho$ is given by $du dQ(\theta)$. We call $L^p(\Omega_\rho)$, $1 \leq p \leq \infty$ the standard function spaces associated to this Riemannian volume.

For any θ in the unit sphere S^2 , we denote by $C(\theta)$ the orthogonal projection of the ball C onto the plane $T(\theta)$. To any function $g \in L^p(\Omega_\rho)$, we associate for each $\theta \in S^2$ a function g_θ defined on the plane $T(\theta)$ by

$$g_\theta(u) = g(u, \theta), \quad \text{for } u \in T(\theta),$$

and we denote by $\|g_\theta\|_p$ the norm of g_θ in $L^p(T(\theta))$.

To define a smooth version of the truncated X-ray transform, let us consider two balls $S_{in} \subset S_{out}$ contained in B_ρ , with radii $r_{in} < r_{out}$ and with the same center $b \in B_\rho$. Let t be a fixed increasing C^∞ function on $[0, 1]$ verifying $0 \leq t(r) \leq 1$, $t(0) = 0$, $t(1) = 1$, and having all its derivatives equal to 0 at the points $r = 0$ and $r = 1$. For each $\theta \in S^2$, the orthogonal projections of the point b and of the balls S_{in}, S_{out}, B_ρ on the plane $T(\theta)$ are the point $b(\theta)$ and the three planar discs $S_{in}(\theta) \subset S_{out}(\theta) \subset B_\rho(\theta)$. Let $r_{in}(\theta) < r_{out}(\theta)$ be the radii of $S_{in}(\theta)$ and $S_{out}(\theta)$. For $u \in B_\rho(\theta)$, we define the function $\lambda_\theta(u)$ by

$$\lambda_\theta(u) = \begin{cases} 1 & \text{if } u \in B_\rho(\theta) \setminus S_{out}(\theta); \\ 0 & \text{if } u \in S_{in}(\theta); \\ t\left(\frac{|u-b(\theta)|}{r_{out}(\theta)-r_{in}(\theta)}\right) & \text{if } u \in S_{out}(\theta) \setminus S_{in}(\theta). \end{cases}$$

Since (u, θ) is in Ω_ρ iff $u \in B_\rho(\theta)$, the function $\lambda(u, \theta) = \lambda_\theta(u)$ is then a well defined C^∞ function on Ω_ρ . For any function g on Ω_ρ , we define the linear operator $\Lambda : g \rightarrow \Lambda g$, by

$$\Lambda g(u, \theta) = \lambda_\theta(u)g(u, \theta) \quad \text{for } (u, \theta) \in \Omega_\rho. \quad (3)$$

We also use the notation $(\Lambda g)_\theta = \lambda_\theta g_\theta$. It follows that the operator $(I - \Lambda)$, where I is the identity operator, is a smoothed truncation operator on functions in Ω_ρ , associated to the two concentric balls $S_{in} \subset S_{out}$ in B_ρ .

We can now apply this construction to the situation where $S_{out} = C$ is any spherical region in B_ρ and $S_{in} = \tilde{C}$ is a smaller ball inside C . Since $1 - \lambda(u, \theta)$ is zero for all rays $r(u, \theta)$ that do not intersect C , we have the identity $(I - \Lambda)Y_C f = Xf - \Lambda Xf$. Hence we define the *smoothed C-truncated* X-ray transform $Z_C f$ of f by

$$Z_C f = (I - \Lambda)Y_C f = Xf - \Lambda Xf. \quad (4)$$

3 ROI reconstruction from truncated projections

In this section, we present an algorithmic approach for the ROI reconstruction of an unknown density function from ROI-truncated projections.

As indicated above, we consider a forward projection operator X modeling the X-ray transform and we assume that there is a ‘black-box’ linear operator X^{-1} which, for a given class of density functions f , reconstructs f exactly from the non-truncated X-ray projections Xf , i.e., if $Xf(u, \theta)$ is known for *all* (u, θ) in Ω_ρ . That is, we assume that the formal identity $X^{-1}Xf = f$ holds for all functions f in a given class (see Section 4.2). Clearly, this does not imply that one can directly reconstruct $1_C f$ (or $1_{\tilde{C}} f$) by applying X^{-1} to the C -truncated X-ray projections $Y_C f$ or their smoother version $Z_C f$.

We will introduce an algorithm which efficiently uses the known global inverse X^{-1} to iteratively reconstruct an approximation of f inside \tilde{C} using only the C -truncated projections $Y_C f$. As indicated in the introduction, our approach for ROI reconstruction from truncated X-ray projections is a refinement of the so-called Iteration Reconstruction-Reprojection algorithm. Our algorithm combines the global inverse X^{-1} with a wavelet-based regularization operator σ to generate approximations of f within the ROI $\tilde{C} \subset C$. Note that σ is *not linear*, in general. We will discuss specific choices and additional assumptions to ensure the convergence of the algorithm in the next section.

Our iterative reconstruction from the truncated data $Y_C f$ is initialized by

setting

$$f_0 = \sigma X^{-1} Z_C f.$$

We next re-project f_0 and split its X-ray transform into a component smoothly truncated by C and a complementary component, as follows:

$$X f_0 = (I - \Lambda) X f_0 + \Lambda X f_0 = Z_C f_0 + \Lambda X f_0,$$

where $Z_C f_0 = (I - \Lambda) Y_C f_0$. Next, we modify $X f_0$ by replacing $Z_C f_0$ with the already computed smoothed C -truncated data $Z_C f = (I - \Lambda) Y_C f$ and we then apply the inverse X^{-1} , which provides the function

$$h_1 = X^{-1} Z_C f + X^{-1} \Lambda X f_0.$$

We generate the next approximation f_1 of f by applying our regularization operator σ to h_1 , yielding

$$f_1 = \sigma h_1 = \sigma(X^{-1} Z_C f + X^{-1} \Lambda X f_0).$$

Repeating this procedure, we generate a sequence of approximations (f_n) of the unknown f by the iterative procedure

$$f_n = \sigma(X^{-1} Z_C f + X^{-1} \Lambda X f_{n-1}). \quad (5)$$

Under appropriate assumptions on f and the regularization operator σ , one expects the sequence (f_n) to converge *inside the ROI* $\tilde{C} \subset C$ to an accurate approximation of the unknown f .

3.1 Continuous vs. discrete formulas.

In Section 4, we will prove that the algorithm presented above converges when X is the X-ray transform defined in Section 2 and X^{-1} is the continuous inverse derived from the back-projection operator. Furthermore, in Section 5, we will provide numerical validation for the convergence of our ROI reconstruction algorithm using different discrete versions of the forward and backward projection operators associated with tomographic reconstruction in the 3D setting.

In many practical tomographic image acquisition schemes, projection data are acquired from different geometric configurations, including: (a) the *parallel-beam* geometry where radiation sources are located on a sphere in

\mathbb{R}^3 surrounding the object of interest; (b) the *cone-beam* geometry where sources are located on a circle (or a half-circle); and (c) the *spiral* geometry where sources are located on a bounded subset of an helix. For each type of such acquisition geometries, there are specific inversion formulas or discrete algorithms that can be used to recover the density function [3]. That is, we can identify a forward discrete operator X and a discrete inverse, denoted by X^{-1} , that are specific to a given acquisition geometry and that, for a given class of density functions, implement an exact or approximate reconstruction when the complete set of projections is known. For example, the operator X^{-1} can implement the spiral tomography inversion formula by Katsevitch [17, 18] or a Cone-Beam inversion formula [19, 20]. The operator X^{-1} can also be a numerical reconstruction algorithm specific to the acquisition geometry at hand or a ‘black-box’ software program with accessible formats to enter geometric parameters, X-ray data inputs, and to output the reconstructed density estimates. For any pair of forward and backward transforms, our formal iterative reconstruction scheme (5) provides an efficient meta-algorithm to transform a global ‘black-box’ inverse X^{-1} into a ROI reconstruction algorithm from *ROI*-truncated X-ray projections. Our numerical tests in Section 5 indicate that the convergence properties that we prove in the continuous setting where X is the X-ray transform hold for various discrete acquisition geometries including spiral and C-arm acquisitions.

3.2 Wavelet-based regularization

Our ROI reconstruction algorithm includes a wavelet-based regularization operator $f \rightarrow \sigma f$ which transforms f into a function belonging to a finite-dimensional approximation space $V \subset L^2(\mathbb{R}^3)$ of large but finite dimension.

Let us briefly recall the main properties of wavelet approximations in $L^2(\mathbb{R}^3)$ (cf. [21]). The main idea of this approach consists in building an orthonormal basis made up of translated and dilated versions of a set of wavelets generators $\{\psi^1, \dots, \psi^L\}$ in $L^2(\mathbb{R}^3)$. That is:

$$\{\Psi_{j,k}^m(x) = 2^{\frac{n_j}{2}} \psi^m(2^j x - k), \quad \text{with } j \in \mathbb{Z}, k \in \mathbb{Z}^3, m = 1, \dots, L\}. \quad (6)$$

For appropriate choices of the wavelets generators $\{\psi^m\}$, the wavelet bases provide highly efficient approximations of piecewise continuous (or piecewise smooth) functions making the wavelet-based approach generally preferable to other standard approximation methods (e.g., Fourier methods) which are

not very local and tend to be less accurate in approximating functions near points of discontinuities, such as edges. With respect to total variation (TV) and other traditional methods, which are also able to accurately approximate piecewise continuous, wavelets have the advantage of providing better approximations for the texture component of the data [22]. Indeed, wavelets provide *optimally efficient* approximations for functions in Besov and Sobolev spaces [21, Ch.9], and these are useful model spaces for typical density functions. Due to these properties, wavelet-based methods have already been successfully employed in several regularization schemes (cf. [23, 24]).

Even though the wavelet basis (6) ranges over a countably infinite set of scales $j \in \mathbb{Z}$, in discrete implementations j will only range over a finite set with the maximal value j_0 corresponding essentially to the resolution level 2^{-j_0} controlling the approximation error. Since we consider functions with compact support inside the ball B_ρ and wavelets of compact support, the parameter k controlling the space location will also vary over a finite range. Thus, for each given j_0 , there is a finite-dimensional wavelet basis which forms an orthonormal basis of $V \subset L^2(\mathbb{R}^3)$. To simplify notation, we use the multi-index $\mu = (j, k, m)$ and denote this orthonormal wavelet basis of the vector space V by $\mathcal{B} = \{\psi_\mu : \mu \in I_N\}$, where I_N is an index set of cardinality N (note that N depends on j_0). Hence, we write the orthogonal projection f_V of $f \in L^2(\mathbb{R}^3)$ into the wavelet approximation space V as

$$f_V = \sum_{\mu \in I_N} \langle f, \psi_\mu \rangle \psi_\mu.$$

3.2.1 Shrinkage of Wavelets Coefficients

Our wavelet-based regularization operator σ is defined as a *shrinkage* operator on the wavelet coefficients $\langle f, \psi_\mu \rangle$ of a real-valued function f with respect to real-valued wavelets $\{\psi_\mu\}_{\mu \in I_N}$:

$$\sigma f = \sum_{\mu \in I_N} s_j(\langle f, \psi_\mu \rangle) \psi_\mu, \quad (7)$$

from $L^2(\mathbb{R}^3)$ into V , where, for each scale parameter j , the *shrinkage function* $s_j : \mathbb{R} \rightarrow \mathbb{R}$ is a C^2 function associated with a threshold $T_j > 0$ satisfying

$$s_j(x) = \begin{cases} x - T_j & \text{if } x > 2T_j, \\ x + T_j & \text{if } x < -2T_j. \end{cases} \quad (8)$$

Obviously, such function s_j is uniformly Lipschitz, i.e., there is a finite constant c_j for which we have the inequality

$$|s_j(x) - s_j(y)| < c_j |x - y| \quad \text{for all } x, y \in \mathbb{R}.$$

Since the sum in (7) is defined over the finite set I_N , we can compute the uniform Lipschitz constant γ simultaneously valid for all functions s_j as

$$\gamma = \max_{j=1, \dots, j_0} c_j.$$

It follows that $|s_j(x) - s_j(y)| < \gamma|x - y|$ for all $x, y \in \mathbb{R}$, $j = 1, \dots, N$. By the observations above we have that, for any two functions $f, g \in L^2(\mathbb{R}^3)$,

$$\|\sigma f - \sigma g\|_2^2 = \sum_{\mu \in I_N} |s_j(\langle f, \psi_\mu \rangle) - s_j(\langle g, \psi_\mu \rangle)|^2 \leq \gamma^2 \sum_{\mu \in I_N} |\langle f, \psi_\mu \rangle - \langle g, \psi_\mu \rangle|^2.$$

Thus, denoting by p_V the orthogonal projection of $L^2(\mathbb{R}^3)$ onto $V \subset L^2(\mathbb{R}^3)$, we conclude that

$$\|\sigma f - \sigma g\|_2 \leq \gamma \|p_V(f - g)\|_2 \leq \gamma \|(f - g)\|_2 \quad \text{for all } f, g \in L^2(\mathbb{R}^3). \quad (9)$$

Since the finite dimensional space V has an orthonormal basis where each basis elements is in $L^\infty(B_\rho)$, one can clearly find a positive constant c such that any function $v \in V$ verifies

$$\|v\|_2 \leq c \|v\|_\infty \quad \text{and} \quad \|v\|_\infty \leq c \|v\|_2.$$

In view of (9), this implies the existence of another constant (still denoted by c) such that

$$\|\sigma f - \sigma g\|_\infty \leq c \|p_V(f - g)\|_\infty \quad \text{for all } f, g \in L^2(\mathbb{R}^3).$$

4 Convergence of the algorithm

We are now ready to discuss the convergence properties of our ROI reconstruction algorithm.

4.1 Function spaces on the space of rays

Recall that Ω_ρ is the differentiable submanifold of the tangent bundle \mathcal{R} associated with those rays which intersect $B_\rho \in \mathbb{R}^3$. We define $\mathcal{L}(B_\rho)$ as the space of functions $f \in L^2(B_\rho)$ with finite norm

$$\|f\|_{\mathcal{L}(B_\rho)} = \|f\|_{L^\infty(B_\rho)} + \|\Delta f\|_{L^\infty(B_\rho)} + \|\Delta^2 f\|_{L^\infty(B_\rho)}, \quad (10)$$

where Δ is the usual Laplace differential operator in \mathbb{R}^3 . We similarly define $\mathcal{L}(\Omega_\rho)$ using the Laplace operator associated to the Riemannian metric of the manifold Ω_ρ . Clearly, $\mathcal{L}(B_\rho)$ and $\mathcal{L}(\Omega_\rho)$ are Banach spaces with the norm defined by (10).

Note that the space $\mathcal{L}(B_\rho)$ contains the Sobolev space $W^{4,\infty}(B_\rho)$; when all partial derivatives of order up to 4 of a function f are in $L^\infty(B_\rho)$ then f is in $\mathcal{L}(B_\rho)$. The same statement is true for $\mathcal{L}(\Omega_\rho)$, when partial derivatives of f are computed in arbitrary smooth local coordinates on the manifold Ω_ρ . We have the following useful observation.

Proposition 1. *The X-ray transform defines three bounded linear operators, all denoted by the same symbol X , mapping $\mathcal{L}(B_\rho)$ into $\mathcal{L}(\Omega_\rho)$, $L^\infty(B_\rho)$ into $L^\infty(\Omega_\rho)$, and $L^2(B_\rho)$ into $L^2(\Omega_\rho)$. Moreover the operator norms of these three linear operators X are controlled by constants depending only on ρ .*

Proof. For $f \in L^2(B_\rho)$, let $g = Xf$ be defined by the integral formula (1). The norm of g in $L^2(\Omega_\rho)$ can be expressed as

$$\|g\|_2^2 = \int_{S^2} \int_{T(\theta)} g_\theta(u)^2 du dQ(\theta). \quad (11)$$

For $(u, \theta) \in \Omega_\rho$, the intersection of the ray $r(u, \theta)$ and the ball B_ρ is an interval $J(u, \theta)$ of length at most 2ρ . Since f is zero outside of B_ρ , we have

$$\|f\|_{L^1(\mathbb{R})} \leq \sqrt{|B_\rho|} \|f\|_{L^2(\mathbb{R})},$$

where $|B_\rho|$ is the volume (Lebesgue measure) of B_ρ . This implies that

$$|g_\theta(u)| \leq \int_{J(u, \theta)} |f(u + t\theta)| dt \leq \sqrt{2\rho} \left(\int_{J(u, \theta)} |f(u + t\theta)|^2 dt \right)^{1/2}.$$

Equation (11) then implies

$$(\|g\|_2)^2 \leq 2\rho \int_{S^2} I(\theta) dQ(\theta), \quad (12)$$

where $I(\theta)$ is the double integral

$$I(\theta) = \int_{T(\theta)} \int_{\mathbb{R}} |f(u + t\theta)|^2 dt du, \quad \text{for each } \theta \in S^2.$$

A change of coordinates by a rotation in \mathbb{R}^3 shows that, for each θ in S^2 , we have

$$I(\theta) \equiv \int_{\mathbb{R}^3} |f(z)|^2 dz = \|f\|_{L^2(B_\rho)}^2.$$

Since $Q(S^2) = 4\pi^2$, inequality (12) then immediately implies:

$$\|Xf\|_{L^2(\Omega_\rho)} = \|g\|_2 \leq 2\pi\sqrt{2\rho} \|f\|_{L^2(B_\rho)}. \quad (13)$$

Similar arguments show that there is a finite constant $c(\rho)$ depending only on ρ such that

$$\|Xf\|_{L^\infty(\Omega_\rho)} \leq c(\rho) \|f\|_{L^\infty(B_\rho)}, \quad \text{for all } f \in L^\infty(B_\rho)$$

and

$$\|Xf\|_{\mathcal{L}(\Omega_\rho)} \leq c(\rho) \|f\|_{\mathcal{L}(B_\rho)}, \quad \text{for all } f \in \mathcal{L}(B_\rho).$$

This concludes the proof.

4.2 Explicit inversion formulas

An analytic inversion formula for the 3D X-ray transform can be derived from the classical Fourier slice theorem [3]. In this section, we derive explicit continuity properties for this inversion formula.

We start by fixing a function $z \rightarrow \theta(z)$ which takes values in the unit sphere S^2 and such that $\langle z, \theta(z) \rangle = 0$ for almost all $z \in \mathbb{R}^3$. For $g \in \mathcal{L}(\Omega_\rho)$, $\theta \in S^2$ and $v \in T(\theta)$, the 2-dimensional Fourier transform \mathcal{F}_θ of g_θ is defined by

$$\mathcal{F}_\theta g_\theta(v) = \int_{T(\theta)} e^{-i\langle v, u \rangle} g_\theta(u) du.$$

Using standard inequalities, a direct computation shows that, for all $\theta \in S^2$,

$$|\mathcal{F}_\theta g_\theta(v)| \leq c (1 + |v|^4)^{-1} \|g\|_{\mathcal{L}(\Omega_\rho)} \quad \text{for all } v \in T(\theta), \quad (14)$$

where the constant c depends only on ρ (and not on g). For all $g \in \mathcal{L}(\Omega_\rho)$, we use the fixed function $\theta(z)$ selected above to define the function $X^{-1}g$ on \mathbb{R}^3 by

$$X^{-1}g(x) = (2\pi)^{-3} \int_{\mathbb{R}^3} e^{i\langle x, z \rangle} \mathcal{F}_{\theta(z)} g_{\theta(z)}(z) dz. \quad (15)$$

In view of (14), we see that, for any $g \in \mathcal{L}(\Omega_\rho)$, the function $X^{-1}g$ is bounded, continuous, and it verifies

$$\|X^{-1}g\|_{L^\infty(\mathbb{R}^3)} \leq c \|g\|_{\mathcal{L}(\Omega_\rho)}, \quad (16)$$

where the new constant c depends only on ρ (but not on g).

Using our notation, the classical Fourier slice theorem [3] states that

$$\mathcal{F}_{\theta(z)}(Xf)_{\theta(z)}(z) = \mathcal{F}f(z)$$

for any $f \in \mathcal{L}(B_\rho)$. Hence, equation (15) explicitly reconstructs $f \in \mathcal{L}(B_\rho)$ once its X -ray transform $g = Xf$ is known for all $(u, \theta) \in \Omega_\rho$. We denote by X^{-1} this explicit inverse operator. The inversion formula (15) involves the arbitrary function $\theta(z)$, but of course always provides the same value for $X^{-1}g$ when $g \in \mathcal{L}(\Omega_\rho)$.

Let \mathcal{F} be the Fourier transform on \mathbb{R}^3 , and for each $\theta \in S^2$ let \mathcal{F}_θ be the 2-dimensional Fourier transform on the tangent plane $T(\theta)$. Equation (15) implies then the relation

$$\mathcal{F}X^{-1}g(z) = \mathcal{F}_{\theta(z)} g_{\theta(z)}(z), \quad \text{for all } z \in \mathbb{R}^3. \quad (17)$$

4.3 Convergence of ROI reconstruction algorithm

We can now prove that, in the continuous formulation of the X-ray transform, the ROI reconstruction algorithm (5) generates a sequence of functions (f_n) which converges to f *inside* the ROI, provided the truncation region $C \subset B_\rho$ is not too small, under mild assumptions on f and the regularization operator σ .

Theorem 1. *Fix an open ball $B_\rho \subset \mathbb{R}^3$, centered at the origin, of finite radius ρ and a vector space $V \subset \mathcal{L}(B_\rho)$ of finite dimension N . Let $\sigma : L^2(\mathbb{R}^3) \rightarrow V$ be a an operator such that $\sigma = \sigma p_V$, where p_V is the orthogonal projection of $L^2(\mathbb{R}^3)$ onto V , and such that σ verifies either one of the two following sublinearity relations:*

$$\|\sigma h - \sigma g\|_\infty \leq c \|p_V(h - g)\|_\infty \quad \text{for all } h, g \in L^\infty(\mathbb{R}^3), \quad (18)$$

$$\|\sigma h - \sigma g\|_2 \leq c_2 \|p_V(h - g)\|_2 \quad \text{for all } h, g \in L^2(\mathbb{R}^3), \quad (19)$$

where c and c_2 are constants which do not depend on h or g .

Let X be the X-ray transform (1) and X^{-1} be its inverse, given by the explicit integral (15). Let $C \subset B_\rho$ be any spherical region, \tilde{C} be another concentric ball with strictly smaller radius and Z_C be the smoothed C -truncated X-ray transform (4). Then, for any f in $\mathcal{L}(B_\rho)$, there exists a quantity $w > 0$ independent of f such that, whenever the residual volume $|B_\rho \setminus C|$ is less than w , the sequence (f_n) given by (5) converges to a limit $\mathcal{A}(f)$ in $L^\infty(B_\rho)$, at exponential speed in the L^∞ -norm.

Moreover, there is a finite constant c_w dependent on w such that

$$\|\mathcal{A}(f) - f\|_\infty \leq c_w \|f - \sigma f\|_\infty,$$

for all $f \in \mathcal{L}(B_\rho)$. In particular, whenever $f = \sigma f \in V$, then the algorithmic reconstruction $\mathcal{A}(f)$ must coincide with f .

The proof of this theorem will be provided in the next section, after a detailed study of the operator X^{-1} .

Remarks. Note that, due to the finite dimensionality of V , if σ verifies either one of the sublinearity relations (18) and (19), then it also satisfies the other one.

In Theorem 1, the spherical truncation region C must be strictly contained in B_ρ and slightly larger than \tilde{C} . Moreover, for the theorem to hold, the volume $|B_\rho \setminus C|$ is required to be ‘small enough’ or, equivalently, the volume of the spherical truncation region $C \subset B_\rho$ must be ‘large enough’. As we will show in Section 5, the numerical tests indicate that, in practice, the critical minimal radius of C for which our ROI reconstruction algorithm converges is fairly small as compared to ρ , which is a favourable situation for radiation exposure reduction.

It is easy to verify that the wavelet-based regularization operators σ defined in Section 3.2 satisfy the assumptions of Theorem 1. In this case, a density function $f \in L^2(\mathbb{R}^3)$ verifies $f = \sigma f$ if and only if $f \in V$ and, for each $\mu \in I_N$, the wavelet coefficient $\langle f, \psi_\mu \rangle$ is either zero or has modulus larger than a threshold $2T_j$ (recall that $\mu = (j, k, m)$). For any such f , when $|B_\rho \setminus C|$ is small enough, Theorem 1 shows that our ROI reconstruction algorithm from C -truncated projections does converge to f in L^∞ -norm. In general, when f is only assumed to be in $L^\infty(B_\rho)$ but is well approximated

by its regularization σf , our ROI reconstruction algorithm is still guaranteed to converge at exponential speed to $\mathcal{A}(f)$ and the reconstruction error $\|\mathcal{A}(f) - f\|_\infty$ is small since it is bounded by a fixed multiple of $\|f - \sigma f\|_\infty$.

In our numerical demonstrations in Section 5, the regularization space $V \subset L^2(\mathbb{R}^3)$, defined as the span of an orthonormal wavelet system of cardinality N , will be chosen so that it can provide sufficiently good approximations for the class of density functions of interest. Even though our theoretical observations are derived using the continuous formulation of the X-ray transform, the numerical experiments of Section 5 show that our ROI reconstruction algorithm performs successfully using truncated data from different discrete 3D acquisition geometries, including spiral and C-arm acquisitions.

Finally, it is easy to see that any bounded linear operator $\sigma : L^2(\mathbb{R}^3) \rightarrow V$ such that $\sigma p_V = \sigma$ satisfies the sublinearity property (18)-(19). In this case, we can derive the following useful corollary of Theorem 1. Recall that the spectral radius $\text{rad}(\mathcal{M})$ of any linear endomorphism \mathcal{M} of V is the supremum of $|\xi_1|, \dots, |\xi_N|$, where the ξ_j are the N eigenvalues of \mathcal{M} . We have the following result.

Corollary 1. *Let $f \in \mathcal{L}(B_\rho)$ and let $V \subset \mathcal{L}(B_\rho)$ be a finite dimensional subspace. Let X be the X-ray transform in \mathbb{R}^3 and X^{-1} be its inverse, given by the explicit integral (15). Let σ be any bounded linear operator mapping $L^2(\mathbb{R}^3)$ into V such that $\sigma p_V = \sigma$. For a given spherical truncation region $C \subset B_\rho$ and a concentric spherical region \tilde{C} strictly contained in C , let $(I - \Lambda)$ be the associated truncation operator defined as in (3) and let $\mathcal{M} = \sigma X^{-1} \Lambda X$, mapping V into V . Then the sequence of iterates (f_n) defined by (5) converges at exponential speed to σf within the ROI \tilde{C} if and only if $\text{rad}(\mathcal{M}^* \mathcal{M}) < 1$.*

4.4 Proof of Theorem 1

Before proving Theorem 1, we need some preparation.

Let X be the X-ray transform and X^{-1} be its inverse defined on $\mathcal{L}(\Omega_\rho)$ by the explicit inversion formula (15). This formula involves an arbitrary function $z \rightarrow \theta(z)$ mapping \mathbb{R}^3 into S^2 with $\langle z, \theta(z) \rangle \equiv 0$. We will now specify the function $\theta(z)$. For any unit vector $\zeta \in S^2$, we will call $EQ(\zeta)$ the ‘equatorial circle’ of all $\eta \in S^2$ such that $\langle \eta, \zeta \rangle = 0$. Fix $\zeta \in S^2$ and $\eta \in EQ(\zeta)$. For $z \in \mathbb{R}^3$, define $\theta(z) \in EQ(\eta)$ by the normalized exterior

product

$$\theta(z) = \begin{cases} \frac{z \times \eta}{|z \times \eta|} & \text{if } z \times \eta \neq 0 \\ \zeta & \text{if } z \times \eta = 0. \end{cases}$$

For each choice of the unit vectors ζ and $\eta \in EQ(\zeta)$, this function $\theta(z)$ can be used into the integral formula (15) to provide a *bona fide* version of $X^{-1}g$ valid for all $g \in \mathcal{L}(\Omega_\rho)$.

We have the following weak continuity estimates for X^{-1} .

Proposition 2. *Let X be the X -ray transform and X^{-1} be its inverse defined on $\mathcal{L}(\Omega_\rho)$ by (15). There are finite constants $c < c^+$ depending only on the radius ρ of B_ρ such that, for all $g \in \mathcal{L}(\Omega_\rho)$ and all $\varphi \in \mathcal{L}(B_\rho)$, we have*

$$|\langle \varphi, X^{-1}g \rangle| \leq c \|\varphi\|_{C^4} \|g\|_{L^2(\Omega_\rho)} < c^+ \|\varphi\|_{C^4} \|g\|_{L^\infty(\Omega_\rho)} \quad (20)$$

and

$$|\langle \varphi, X^{-1}g \rangle| \leq c \|\varphi\|_{C^4} \int_{EQ} \|g_\theta\|_2 d\theta, \quad (21)$$

where EQ is any equatorial (great) circle of S^2 and $\langle \cdot, \cdot \rangle$ is the inner product on $L^2(\mathbb{R}^3)$.

Proof. For $\varphi \in \mathcal{L}(B_\rho)$ and $g \in \mathcal{L}(\Omega_\rho)$, equation (17) implies

$$\langle \varphi, X^{-1}g \rangle = \langle \mathcal{F}\varphi, \mathcal{F}X^{-1}g \rangle = \int_{\mathbb{R}^3} \mathcal{F}\varphi(z) \mathcal{F}_{\theta(z)} g_{\theta(z)}(z) dz. \quad (22)$$

For any $\eta \in S^2$ and any function $h \in L^1(\mathbb{R}^3)$, integration in cylindrical coordinates around the rotation axis η shows that

$$\int_{\mathbb{R}^3} h(z) dz = \frac{1}{2} \int_{EQ(\eta)} \int_{T(\theta)} h(v) |\langle v, \eta \times \theta \rangle| dv d\theta,$$

where $EQ(\eta)$ is the equatorial circle. Hence equation (22) becomes

$$\begin{aligned} \langle \varphi, X^{-1}g \rangle &= \frac{1}{2} \int_{EQ(\eta)} \int_{T(\theta)} |\langle v, \eta \times \theta \rangle| \mathcal{F}\varphi(v) \mathcal{F}_\theta g_\theta(v) dv d\theta \\ &= \frac{1}{2} \int_{EQ(\eta)} \langle g_\theta, \mathcal{F}_\theta g_\theta \rangle d\theta, \end{aligned} \quad (23)$$

where, for each $\theta \in S^2$, the function $g_\theta \in L^2(T(\theta))$ is given by

$$g_\theta(v) = |\langle v, \eta \times \theta \rangle| \mathcal{F}\varphi(v), \quad v \in T(\theta).$$

In view of the bound for $|\mathcal{F}\varphi(v)|$ given by (14), the function g_θ must satisfy

$$\|g_\theta\|_2 \leq c \|\varphi\|_{C^4} \quad \text{for all } \theta \in EQ(\eta), \quad (24)$$

where the new constant c does not depend on φ or η . Equation (23) shows that

$$|\langle \varphi, X^{-1}g \rangle| \leq \frac{1}{2} \int_{EQ(\eta)} \|g_\theta\|_2 \|\mathcal{F}_\theta g_\theta\|_2 d\theta.$$

By inequality (24), the last relation proves that there is a constant c such that, for all $g \in \mathcal{L}(\Omega_\rho)$, all $\varphi \in \mathcal{L}(B_\rho)$ and all unit vectors η , we have that

$$|\langle \varphi, X^{-1}g \rangle| \leq c \|\varphi\|_{C^4} \int_{EQ(\eta)} \|g_\theta\|_2 d\theta.$$

This proves (21). Now, keeping the unit vector ζ and the associated equatorial circle $EQ(\zeta)$ fixed, we let the unit vector η vary within the circle $EQ(\zeta)$, we multiply both sides of (21) by a non-negative function $u(\eta)$ such that $u(\eta) = u(-\eta)$ and we integrate over all $\eta \in EQ(\zeta)$ to obtain

$$|\langle \varphi, X^{-1}g \rangle| \int_{EQ(\zeta)} u(\eta) d\eta \leq c \|\varphi\|_{C^4} \int_{EQ(\zeta)} u(\eta) \int_{EQ(\eta)} \|g_\theta\|_2 d\theta d\eta. \quad (25)$$

Fix any η_0 in $EQ(\zeta)$ and let $\theta_0 = \zeta \times \eta_0$. For any $\eta \in EQ(\zeta)$ and $\theta \in EQ(\eta)$, let α be the angle between η and η_0 and β the angle between θ and θ_0 . Then the two angles $(\alpha, \beta) \in [0, 2\pi] \times [0, 2\pi]$ uniquely determine $\eta = \eta(\alpha)$ and $\theta = \theta(\alpha, \beta) \in S^2$. The function $(\alpha, \beta) \rightarrow \theta(\alpha, \beta)$ is the one-to-one mapping of $[0, \pi] \times [0, 2\pi]$ onto the unit sphere S^2 defined by the classical spherical coordinates (α, β) on S^2 . The same statement holds for (α, β) in $[\pi, 2\pi] \times [0, 2\pi]$. The function $u(\eta)$ is mapped to any non-negative function $U(\alpha)$ such that $U(\alpha) = U(\alpha + \pi)$.

Letting $A(\theta) = \|g_\theta\|_2$, we can now rewrite inequality (25) as

$$|\langle \varphi, X^{-1}g \rangle| \int_0^{2\pi} U(\alpha) d\alpha \leq c \|\varphi\|_{C^4} \int_0^{2\pi} U(\alpha) \int_0^{2\pi} A(\theta(\alpha, \beta)) d\beta d\alpha. \quad (26)$$

In the spherical coordinates (α, β) , the element of area on S^2 is equal to $|\sin(\alpha)| d\alpha d\beta$. Call Q the associated surface measure on S^2 and select $U(\alpha) = |\sin(\alpha)|$. We then have:

$$\int_0^\pi |\sin(\alpha)| \int_0^{2\pi} A(\theta(\alpha, \beta)) d\beta d\alpha = \int_{S^2} A(\theta) dQ(\theta),$$

and the same result holds if we replace the interval of integration $[0, \pi]$ by $[\pi, 2\pi]$. Hence, for the specific choice $U(\alpha) = |\sin(\alpha)|$, inequality (26) gives that

$$4 |\langle \varphi, X^{-1}g \rangle| \leq 2c \|\varphi\|_{C^4} \int_{S^2} A(\theta) dQ(\theta). \quad (27)$$

The Cauchy-Schwarz inequality yields

$$\left| \int_{S^2} A(\theta) dQ(\theta) \right|^2 \leq Q(S^2) \int_{S^2} A(\theta)^2 dQ(\theta). \quad (28)$$

By construction, $A(\theta)^2 = \int_{T(\theta)} g(v, \theta)^2 dv$. Hence, inequality (28) implies that

$$\left| \int_{S^2} A(\theta) dQ(\theta) \right|^2 \leq 4\pi^2 \int_{S^2} \int_{T(\theta)} g(v, \theta)^2 dv dQ(\theta) = 4\pi^2 \|g\|_{L^2(\Omega_\rho)}^2. \quad (29)$$

Combining (29) with (27) yields the existence of a constant c such that

$$|\langle \varphi, X^{-1}G \rangle| \leq c \|\varphi\|_{C^4} \|g\|_{L^2(\Omega_\rho)}, \quad (30)$$

for all $g \in \mathcal{L}(\Omega_\rho)$ and all $\varphi \in \mathcal{L}(B_\rho)$. Since Ω_ρ is a relatively compact set, there exists a constant c_ρ depending only on ρ such that

$$\|g\|_{L^2(\Omega_\rho)} < c_\rho \|g\|_{L^\infty(\Omega_\rho)}, \quad (31)$$

for all $g \in \mathcal{L}(\Omega_\rho)$. Inequality (20) follows by combining (31) and (30). \square

We are now ready to prove Theorem 1.

Proof of Theorem 1.

Let $|B_\rho(\theta) \setminus C(\theta)|$ be the surface area of the planar corona $B_\rho(\theta) \setminus C(\theta)$ in the plane $T(\theta)$. By construction, we have $0 \leq \lambda_\theta \leq 1_{B_\rho(\theta) \setminus C(\theta)}$. Hence, for all $\theta \in S^2$ and all functions $g \in L^\infty(\Omega_\rho)$, we have

$$\|(\Lambda g)_\theta\|_2 \leq \sqrt{|B_\rho(\theta) \setminus C(\theta)|} \|g_\theta\|_\infty. \quad (32)$$

Let $h \in V$. By (32) and the elementary observation that, for each $\theta \in S^2$, $\|Xh_\theta\|_\infty \leq 2\rho \|h\|_\infty$, it follows that the function ΛXh satisfies

$$\|(\Lambda Xh)_\theta\|_2 \leq \sqrt{|B_\rho(\theta) \setminus C(\theta)|} \|(Xh)_\theta\|_\infty \leq 2\rho \sqrt{|B_\rho(\theta) \setminus C(\theta)|} \|h\|_\infty. \quad (33)$$

Hence, for any $\varphi \in \mathcal{L}(B_\rho)$, using inequalities (21) and (33), we obtain that

$$|\langle \varphi, X^{-1}\Lambda X h \rangle| \leq c \|\varphi\|_{C^4} \|h\|_\infty \int_{EQ} \sqrt{|B_\rho(\theta) \setminus C(\theta)|} d\theta \quad (34)$$

for any equatorial circle EQ of S^2 . For any function f on the equatorial circle EQ , due to the compactness of the support, we have that $\|f\|_1 \leq \sqrt{2\pi} \|f\|_2$ and, hence,

$$\int_{EQ} \sqrt{|B_\rho(\theta) \setminus C(\theta)|} d\theta \leq \sqrt{2\pi} \left(\int_{EQ} |B_\rho(\theta) \setminus C(\theta)| d\theta \right)^{1/2} = \sqrt{2\pi |B \setminus C|}.$$

Thus, inequality (34) implies that, for any functions φ and h in $\mathcal{L}(B_\rho)$, we have that

$$|\langle \varphi, X^{-1}\Lambda X h \rangle| \leq c \sqrt{|B \setminus C|} \|\varphi\|_{C^4} \|h\|_\infty, \quad (35)$$

where the new constant c depends on ρ but not on φ or h .

Let p_V be the orthogonal projection of $L^2(\mathbb{R}^3)$ onto the vector subspace V . By hypothesis, V has an orthonormal basis $(\varphi_1, \dots, \varphi_N)$ of cardinality N , where each φ_i belongs to $\mathcal{L}(B_\rho)$. Applying (35) to each φ_i yields that

$$\|p_V X^{-1}\Lambda X h\|_\infty \leq \left\| \sum_{i=1, \dots, N} \langle \varphi_i, X^{-1}\Lambda X h \rangle \right\|_\infty \leq cN \sqrt{|B \setminus C|} \kappa \|h\|_\infty, \quad (36)$$

for any h in $\mathcal{L}(B_\rho)$, where the constants c and $\kappa = \max_{i=1, \dots, N} \|\varphi_i\|_{C^4}$ do not depend on h .

Algorithm (5) generates a sequence of functions $(f_n) \in V$ given by the recursive relation

$$f_n = \sigma (X^{-1}Z_C f + X^{-1}\Lambda X f_{n-1}).$$

The two functions

$$k = X^{-1}Z_C f + X^{-1}\Lambda X f_n \text{ and } g = X^{-1}Z_C f + X^{-1}\Lambda X f_{n-1}$$

then verify

$$f_{n+1} - f_n = \sigma k - \sigma g \text{ and } p_V(k - g) = p_V X^{-1}\Lambda X(f_n - f_{n-1}).$$

Thus, by applying to k and g the inequality (18), we obtain

$$\|f_{n+1} - f_n\|_\infty \leq c \|p_V X^{-1}\Lambda X(f_n - f_{n-1})\|_\infty,$$

valid for all integers $n \geq 0$. Combining this last inequality with (36), evaluated for $h = f_{n+1} - f_n$, we see that there is a constant c such that

$$\|f_{n+1} - f_n\|_\infty \leq c \sqrt{|B \setminus C|} \|(f_n - f_{n-1})\|_\infty, \quad \text{for all integers } \geq 0.$$

Thus, if $\sqrt{|B \setminus C|}$ is smaller than β/c where $\beta < 1$ is fixed, we have

$$\|f_{n+1} - f_n\|_\infty \leq \beta^n \|f_1 - f_0\|_\infty \quad \text{for all } n \geq 0. \quad (37)$$

Since on the vector space V the L^2 -norm and L^∞ -norm are equivalent and since $f_n \in V$ for all n , inequality (37) implies that

$$\|f_{n+1} - f_n\|_2 \leq c \beta^n \|f_1 - f_0\|_2 \quad \text{for all } \geq 0.$$

Thus, the sequence (f_n) must converge at exponential speed in $L^\infty(B_\rho)$ and in $L^2(B_\rho)$ to a limit $\mathcal{A}(f)$ belonging to $L^\infty(B_\rho) \subset L^2(B_\rho)$.

By taking the limit as $n \rightarrow \infty$ in (5), we then have

$$\mathcal{A}(f) = \lim_{n \rightarrow \infty} f_n = \sigma(X^{-1}Z_C f + X^{-1}\Lambda X \mathcal{A}(f)).$$

By (4), the last equation implies that

$$\mathcal{A}(f) = \sigma(f - X^{-1}\Lambda X f + X^{-1}\Lambda X \mathcal{A}(f)).$$

We also have the obvious identity

$$\sigma f = \sigma(f - X^{-1}\Lambda X f + X^{-1}\Lambda X f).$$

Thus, the two functions

$$\tilde{k} = f - X^{-1}\Lambda X f + X^{-1}\Lambda X \mathcal{A}(f) \quad \text{and} \quad \tilde{g} = f - X^{-1}\Lambda X f + X^{-1}\Lambda X f$$

verify

$$\mathcal{A}(f) - \sigma f = \sigma \tilde{k} - \sigma \tilde{g} \quad \text{and} \quad p_V(k - g) = p_V X^{-1} \Lambda X (\mathcal{A}(f) - f).$$

By applying inequality (18) to \tilde{k} and \tilde{g} we have that

$$\|\mathcal{A}(f) - \sigma f\|_\infty \leq c \|p_V X^{-1} \Lambda X (\mathcal{A}(f) - f)\|_\infty. \quad (38)$$

By (36), is a constant c such that

$$\|p_V X^{-1} \Lambda X (\mathcal{A}(f) - \sigma f)\|_\infty \leq c \sqrt{|B_\rho \setminus C|} \|\mathcal{A}(f) - f\|_\infty.$$

Thus, combining this inequality with (38), it follows that there is a (new) constant c such that

$$\|\mathcal{A}(f) - \sigma f\|_\infty \leq c \sqrt{|B_\rho \setminus C|} \|(\mathcal{A}(f) - f)\|_\infty. \quad (39)$$

Now we require the truncation region C to be large enough to verify the inequality $\sqrt{|B_\rho \setminus C|} < \beta/c$ for all constants c introduced above, for some fixed $\beta < 1$. Inequality (39) then implies

$$\|\mathcal{A}(f) - \sigma f\|_\infty \leq \beta \|(\mathcal{A}(f) - f)\|_\infty \leq \beta (\|\mathcal{A}(f) - \sigma f\|_\infty + \|\sigma f - f\|_\infty)$$

and this obviously yields

$$\|\mathcal{A}(f) - \sigma f\|_\infty \leq \frac{\beta}{1 - \beta} \|\sigma f - f\|_\infty$$

and, hence,

$$\|\mathcal{A}(f) - f\|_\infty \leq \|\mathcal{A}(f) - \sigma f\|_\infty + \|\sigma f - f\|_\infty \leq \frac{1}{1 - \beta} \|\sigma f - f\|_\infty.$$

This proves the last statement of the theorem and concludes the proof. \square

5 Numerical experiments

In this section, we present several numerical experiments to illustrate the convergence properties of our ROI reconstruction algorithm (5) from Section 3. Even though our theoretical analysis is limited to the continuous setting of the X-ray transform, here we consider different discrete transforms with simulated acquisitions corresponding to various practical settings. As our experiments will show, our general theoretical observations such as the existence of a critical ROI radius ensuring the algorithm convergence appear to hold even in the discrete setting under more realistic acquisition schemes. The purpose of this section is not a full validation of our ROI reconstruction approach with an actual CT device, but rather the numerical verification that our theoretical predictions hold in the discrete setting.

For all our experiments, we have used simulated acquisition and considered the following data sets: a 3D Shepp-Logan phantom; a 3D scan of a mouse; a 3D scan of a human jaw. For each set, the size was 256^3 voxels. Each

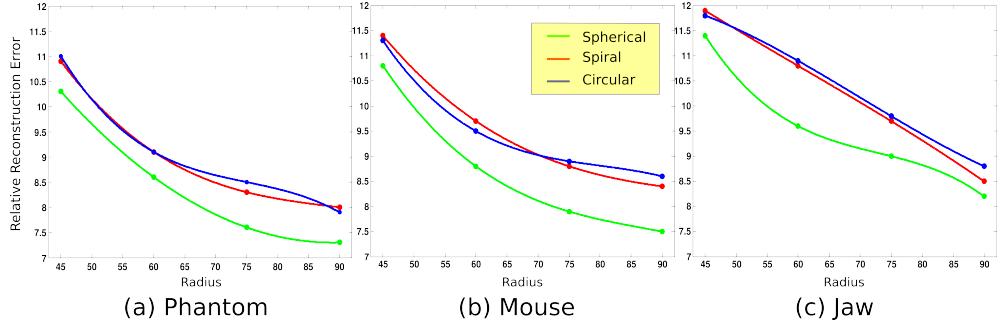


Figure 2: Plots of the Relative Reconstruction Errors in the ROI using different discrete forward and backward transforms, with simulated acquisition. The three panels show the Relative Reconstruction Errors in the ROI for the three data sets described in the text: (a) Shepp-Logan phantom; (b) mouse tissue; (c) human jaw. ROI radius=50 voxels.

time, we have computed full scans with complete projections; next we have truncated the projection data by applying a discrete version of the smoothed truncation operator given by equation (4) on the projected data. We have simulated full data acquisitions using different discrete forward and inverse transforms: (i) parallel beam and filtered back-projection (FBP); (ii) spiral tomography and the corresponding Katsevich inversion formula; C-arm tomography curve with sources along a circular curve and corresponding FBP. In the simulated acquisition, we have set the scanning radius to 384 voxels for the spiral acquisition and 400 voxels for the parallel-beam and circular cases. We have set the number of detector rows to 16 for the spiral, 100 for the circular and 256 for the parallel-beam acquisition and we have set the spacing of the source positions to be at 1 degree intervals for the circular case. In the parallel-beam case the discretization was 3 degrees in the polar direction and 5 degrees in the azimuthal direction. For the spiral acquisition we have chosen a total of 128 source positions in every complete turn and set the helical pitch to 35 voxels leading to approximately 8 turns to scan the whole object. Finally we have set the source-detector distance at 768 voxels for the spiral case and 900 voxels for the other two cases.

To validate the existence of a critical radius of convergence, as predicted by Theorem 1 and Corollary 1 under very general conditions, we have considered multiple spherical ROIs, centered at varying locations inside the support of unknown density function f and with varying ROI radii. Recall that The-

orem 1 predicts that – in the continuous setting of the X-ray transform – the algorithm converges if the ROI radius is sufficiently large, but does not indicate how to choose such radius. We found through numerical testing that, for data of the size indicated above, the radius of 45 voxels is the minimal radius needed to ensure that our algorithm converges to accurate ROI reconstructions, which is rather small (see further comments in the next section). For all our experiments, we stopped our algorithm after 40 iterations as this number was found to ensure the convergence of the algorithm.

For the regularization operator σ , we have used the wavelet-based approach described in Section 3.2 based on the shrinkage operator (7), where the thresholding constants T_j in (8) depend on the scale parameter j . For the fine scales, $j > 1$, we have set the values T_j in such a way that 90% of wavelet coefficients were set to zero. No shrinkage was applied at the coarsest scales since they contain the global information and the modification of these coefficients would affect the solution inside the region of interest. For the wavelet decomposition, we have used standard Daubechies wavelets Daub4 [21] that ensure both regularization performance and computational efficiency (due to the small support size).

5.1 Numerical Analysis of Contractivity

Based on the conclusions of Corollary 1, it is useful to examine the convergence properties of our algorithm through the numerical analysis of the operator norm ρ of the matrix $\mathcal{M} = \sigma X^{-1} \Lambda X$ associated with the algorithm (5).

To make this computation feasible with a PC, we have considered matrices of small data size. Specifically, we have examined 3D discrete density functions supported in a cube B of 64^3 voxels. This implies that the density function can be viewed as a 3D image and hence as a vector in \mathbb{R}^{262144} . We have considered the standard basis in this space, i.e., the set of matrices E_{ijk} whose entries are 1 at the (i, j, k) -th position and zeros everywhere else. We have considered regions of interest with radii between 6 and 22 voxels and calculated the spectral radius for the operator $\mathcal{M}^* \mathcal{M}$, where $\mathcal{M} = \sigma X^{-1} \Lambda X$ and X, X^{-1} are the forward and backward transforms, respectively, for the various discrete formulas considered.

The results in Table 1 show that the contractivity of the matrix \mathcal{M} is ensured if the ROI radius is at least 14 voxels. Note the abrupt transition from non contracting \mathcal{M} to contracting \mathcal{M} when the ROI radius changes

Table 1: Spectral radius of $(\mathcal{M}^* \mathcal{M})^{\frac{1}{2}}$ for various ROI-radii (image size is 64^3)

ROI-radius	6	10	13	14	18	22
Parallel Beam	10.62	9.33	4.15	0.90	0.74	0.66
Spiral CT	15.27	8.54	4.07	0.94	0.83	0.73
Circular CT	16.53	9.49	4.36	0.97	0.89	0.77

from 13 to 14 voxels. This condition on the spectral radius is independent of the data and depends only on the data size, the ROI and the techniques of acquisition, inversion and regularization. By extrapolating from these results, we deduce that, for objects of size 256^3 , the contractivity of \mathcal{M} would be ensured provided the ROI radius is about 55 voxels. This number is not very far from the value of 45 voxels which, as mentioned above, was found to ensure numerical convergence in our experiments.

5.2 Algorithm Performance

To assess the accuracy of reconstruction provided by our algorithm, we have used the notion of *Relative Reconstruction Error*, defined as follows. Let f be the density function to be recovered, where f is assumed to be a bounded function with compact support in \mathbb{R}^3 ; let f_{rec} be an approximate reconstruction of f ; and let C be a spherical region inside the support of f . The Relative Reconstruction Error Rel in the region C is the number

$$Rel = \int_C \frac{|f(v) - f_{rec}(v)|}{|f(v)|} dv.$$

Figure 2 plots the Relative Reconstruction Errors within the ROI, as functions of the ROI radius, for the different density data we have studied. Each plot displays three curves, one curve for each one of the three discrete forward and backward transform formulas we have considered. Note that the best performance of the algorithm occurs in the case of parallel-beam acquisition, due to the fact that the larger number of projections makes the reconstruction from incomplete data more robust in this case. The performance of the algorithm is comparable in the cases of spiral and circular acquisitions. Also note that, for a fixed ROI radius, the Relative Reconstruction Error in the ROI is lower in the case of phantom data and higher in the case of mouse and jaw data. This is due to the different regularity properties of the data and can be explained as follows.

As observed in the comments following the statement of Theorem 1, the ROI reconstruction algorithm converges to a regularized approximation σf rather than to the exact density function f in the ROI. As a consequence, the Relative Reconstruction Error in the ROI can be broken up into two additive components, one due to the convergence error (since we use only finitely many iterations) and another one due to the difference between f and σf . To highlight the effect of the regularization, we have computed the component of the relative reconstruction error in the ROI due to the regularization only, that is,

$$Rel_\sigma = \int_C \frac{|f(v) - (\sigma f)(v)|}{|f(v)|} dv.$$

For the phantom data, we have found that this error is $Rel_\sigma = 1.1\%$, while, for the mouse and jaw data sets, we have found $Rel_\sigma = 2.4\%$. For example, in Figure 2, for ROI radius = 70, in the case of parallel-beam acquisition, the Relative Reconstruction Error $Rel \approx 8\%$ in the ROI for the Phantom data is approximately the sum of $Rel_\sigma = 1.1\%$ plus a term due to the convergence error $\approx 7\%$. In the case of Jaw data the two parts are approximately 2.4% and 6.6%. The lower value Rel_σ in the case of Phantom data is explained by the observations that the piecewise constant data can be approximated by the wavelet-based regularization operator much more effectively than the more complex mouse and jaw data.

To illustrate the overall quality of our ROI reconstruction algorithm from truncated projections we have included some examples in Figures 3-8 for the Phantom and Mouse data. The figures show a baseline comparison of the ROI reconstructions obtained using our algorithm versus the standard unregularized reconstructions computed using the appropriate full-scan discrete inversion formulas applied to truncated projection data. Each figure shows the horizontal middle slice extracted from the reconstructed 3D volumes in the cases of simulated acquisitions using parallel-beam, spiral and circular acquisition modes. As expected, the standard unregularized ROI reconstructions from truncated projections are inaccurate and contain several visual artifacts especially near the boundary of the ROI. By contrast, the reconstruction results provided by our algorithm are very satisfactory even for relatively small ROI radii.



Figure 3: Visual comparison of ROI reconstruction for the 3D Shepp-Logan phantom using simulated parallel-beam acquisition and truncation of projection data. A representative 2D slice from the 3D volume is shown. From left to right: unregularized FBP reconstruction; regularized ROI CT reconstruction (our algorithm); ground truth.



Figure 4: Visual comparison of ROI reconstruction for the 3D Shepp-Logan phantom using simulated spiral acquisition and truncation of projection data. A representative 2D slice from the 3D volume is shown. From left to right: unregularized reconstruction using Katsevich inversion algorithm; regularized ROI CT reconstruction (our algorithm); ground truth.



Figure 5: Visual comparison of ROI reconstruction for the 3D Shepp-Logan phantom using simulated circular acquisition and truncation of projection data. A representative 2D slice from the 3D volume is shown. From left to right: unregularized reconstruction using appropriate FBP algorithm; regularized ROI CT reconstruction (our algorithm); ground truth.

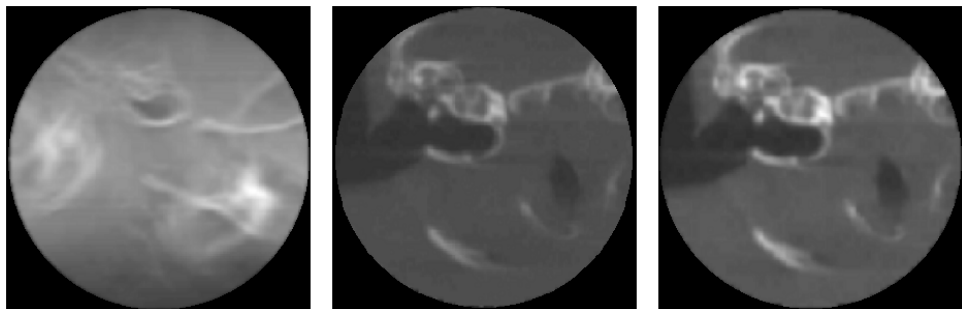


Figure 6: Visual comparison of ROI reconstruction for mouse 3D scan data using simulated parallel-beam acquisition and truncation of projection data. A representative 2D slice from the 3D volume is shown. From left to right: unregularized FBP reconstruction; regularized ROI CT reconstruction (our algorithm); ground truth.

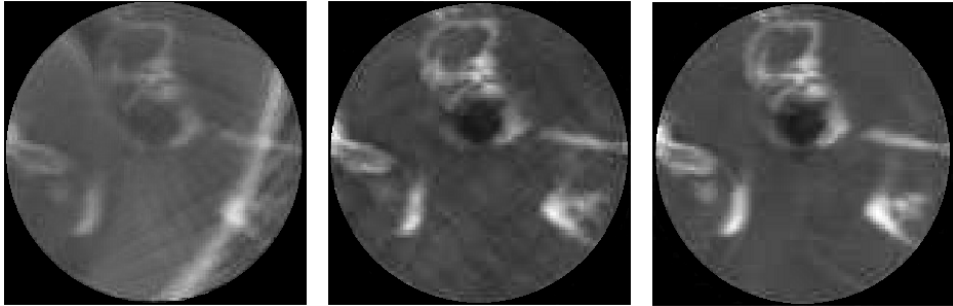


Figure 7: Visual comparison of ROI reconstruction for mouse 3D scan data using simulated spiral acquisition and truncation of projection data. A representative 2D slice from the 3D volume is shown. From left to right: unregularized reconstruction using Katsevich inversion algorithm; regularized ROI CT reconstruction (our algorithm); ground truth.

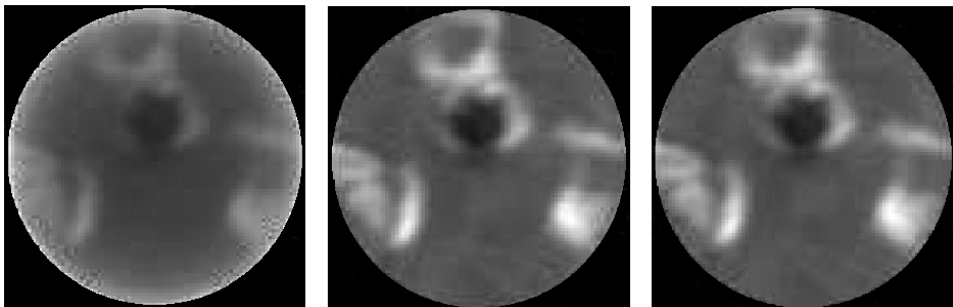


Figure 8: Visual comparison of ROI reconstruction for mouse 3D scan data using simulated circular acquisition and truncation of projection data. A representative 2D slice from the 3D volume is shown. From left to right: unregularized reconstruction using appropriate FBP algorithm; regularized ROI CT reconstruction (our algorithm); ground truth.

6 Convolution based ROI reconstruction

We now outline an alternative ROI reconstruction algorithm from truncated X-ray data. At each iterative step, regularization will now be implemented by a *linear* operator of *convolution type* acting on the *space of rays* Ω_ρ , instead of applying a *non-linear* wavelet-based shrinkage operator on the image space \mathbb{R}^3 as studied above. In the following, we prove convergence of this convolution-based ROI reconstruction scheme and evaluate its reconstruction error in $L^2(\mathbb{R}^3)$ norm.

6.1 Convolution kernels on the space of rays

The group \mathcal{J} of all isometries J of \mathbb{R}^3 is generated by translations and rotations, and hence acts naturally on the manifold Ω_ρ of all rays. Thus Ω_ρ can be identified to the homogeneous space $\mathcal{J}/\mathcal{J}_0$ where \mathcal{J}_0 is the 1-dimensional subgroup of all translations parallel to a fixed arbitrary unit vector $\theta_0 \in S$. Any positive measure τ of mass 1 on \mathcal{J} then acts linearly on the space $L^2(\Omega_\rho)$ by natural left-convolutions. Namely for any function $g \in L^2(\Omega_\rho)$ one defines $\tau * g$ by

$$\tau * g(u, \theta) = \int_{\mathcal{J}} g(J(u, \theta)) d\tau(J) \quad \text{for all rays } (u, \theta) \in \Omega_\rho$$

We now apply this geometric framework to define explicitly natural families of smoothing linear kernels K_s , indexed by $s > 0$, acting on $L^2(\Omega_\rho)$ by left-convolutions, and which approximate the identity in $L^2(\Omega_\rho)$ as $s \rightarrow 0$. Fix a non-negative C^∞ radial function $\kappa(|z|)$ of $z \in \mathbb{R}^3$, with support in the unit ball of \mathbb{R}^3 , and such that $\int_{\mathbb{R}^3} \kappa(|z|) dz = 1$.

For any ray $(u, \theta) \in \Omega_\rho$, the vector u is in the plane $T(\theta)$ orthogonal to θ , and hence for any $y \in \mathbb{R}^3$ the vector $v = u - y + \langle y, \theta \rangle \theta$ is also in $T(\theta)$, so that (v, θ) is in Ω_ρ . For each $s > 0$ and each $g \in L^\infty(\Omega_\rho)$, we can then define the function $h = K_s g$ for all $(u, \theta) \in \Omega_\rho$ by

$$h_\theta(u) = K_s g(u, \theta) = \frac{1}{s^3} \int_{\mathbb{R}^3} \kappa(|y|/s) g(u - y + \langle y, \theta \rangle \theta, \theta) dy. \quad (40)$$

The linear operators K_s map $L^\infty(\Omega_\rho)$ into $L^2(\Omega_\rho)$, and are naturally linked to the standard *convolution operators* μ_s on \mathbb{R}^3 defined for all f in $L^\infty(\mathbb{R}^3)$ by

$$\mu_s * f(z) = \frac{1}{s^3} \int_{\mathbb{R}^3} \kappa(|x|/s) f(z - x) dx. \quad (41)$$

When $s \rightarrow 0$, the convolution operators μ_s are natural approximations of the identity in $L^p(\mathbb{R}^3)$ for any $p \geq 1$. Moreover for any $s > 0$ and any $f \in L^\infty(B_\rho)$, the X-ray transform X verifies the “commutation” relation

$$K_s X f = X \mu_s * f. \quad (42)$$

Fix any ray (u, θ) in Ω_ρ , so that $u \in T(\theta)$. The integral giving $h = K_s g$ in equation (40) can be computed by the change of variable $y \rightarrow (w, \lambda)$ where $w = y - \langle y, \theta \rangle \theta$ is in $T(\theta)$ and $\lambda = \langle y, \theta \rangle$ is in \mathbb{R} , so that $y = w + \lambda \theta$. We then have $dy = dw d\lambda$ and the integral becomes

$$h_\theta(u) = K_s g(u, \theta) = \frac{1}{s^3} \int_{T(\theta)} \left[\int_{\mathbb{R}} \kappa(|w + \lambda \theta|/s) d\lambda \right] g(u - w, \theta) dw,$$

which can clearly be rewritten as

$$h_\theta(u) = K_s g(u, \theta) = \frac{1}{s^2} \int_{T(\theta)} \gamma(|w|/s) g(u - w, \theta) dw, \quad (43)$$

where the non-negative C^∞ radial function γ is defined for all $v \in \mathbb{R}^3$ by the integral

$$\gamma(v) = \int_{\mathbb{R}} \kappa((|v|^2 + t^2)^{1/2}) dt. \quad (44)$$

In particular, for any $\theta \in S^2$, we have $\int_{T(\theta)} \gamma(v) dv = 1$ and $\gamma(v) = 0$ for $|v| \geq 1$. Denote $\gamma_s(v) = \frac{1}{s^2} \gamma(v/s)$ and recall the notation $g_\theta(u) = g(u, \theta)$. Then equation (43) shows that, for each $\theta \in S^2$, the function $h_\theta(u) = K_s g(u, \theta)$ can be obtained by a standard two-dimensional convolution on the plane $T(\theta)$, namely by

$$h_\theta = \gamma_s * g_\theta.$$

Let Ω_ρ be the set of all rays which do intersect the ball B_ρ . Since γ_s is non-negative and has integral 1, the convexity of the unit ball of $L^2(T(\theta))$ implies that $\|h_\theta\|_{L^2(T(\theta))} \leq \|g_\theta\|_{L^2(T(\theta))}$. Denoting by $dQ(\theta)$ the element of surface area on the sphere S^2 , we have then, by (11),

$$\|K_s g\|_{L^2(\Omega_{\rho+s})}^2 = \int_{S^2} \|h_\theta\|_{L^2(T(\theta))}^2 dQ(\theta) \leq \int_{S^2} \|g_\theta\|_{L^2(T(\theta))}^2 dQ(\theta) = \|g\|_{L^2(\Omega_\rho)}^2. \quad (45)$$

Since g is non-zero in Ω_ρ only, the essential support of g_θ in $T(\theta)$, denoted as $\text{spt } g_\theta$ below, is always included in a planar disk of radius ρ .

6.2 Convolution based ROI reconstruction

We now define a *new iterative ROI reconstruction* algorithm, called here “convolution-based”, as follows. Let $f \in L^\infty(B_\rho)$ be an unknown density function on \mathbb{R}^3 and, as above, assume that our only available data are the truncated projections $g = \mathbf{1}_{\mathcal{R}_C} X f$, where $\mathcal{R}_C \subset \Omega_\rho$ is the set of rays intersecting the ball $C \subset B_\rho$.

Let $\mathbf{1}_{B_\rho}$ be the indicator function of the ball B_ρ . We initialize the reconstruction algorithm by setting

$$f_0 = \mathbf{1}_{B_\rho} X^{-1} K_s g = \mathbf{1}_{B_\rho} X^{-1} K_s \mathbf{1}_{\mathcal{R}_C} X f.$$

Next we re-project f_0 and split the resulting quantity as follows

$$X f_0 = (I - \mathbf{1}_{\mathcal{R}_C}) X f_0 + \mathbf{1}_{\mathcal{R}_C} X f_0.$$

We replace $\mathbf{1}_{\mathcal{R}_C} X f_0$ by the known truncated data $g = \mathbf{1}_{\mathcal{R}_C} X f$ to get

$$\widetilde{X f_0} = (I - \mathbf{1}_{\mathcal{R}_C}) X f_0 + g.$$

Now we regularize $\widetilde{X f_0}$ by the smoothing operator K_s , before applying the inverse transform X^{-1} , to obtain

$$X^{-1} K_s [(I - \mathbf{1}_{\mathcal{R}_C}) X f_0 + g].$$

Finally, a restriction to the ball B_ρ yields

$$f_1 = \mathbf{1}_{B_\rho} X^{-1} K_s [(I - \mathbf{1}_{\mathcal{R}_C}) X f_0 + g].$$

Iterating the preceding procedure recursively defines the successive approximate density reconstructions f_n by

$$f_n = M f_{n-1} + \mathbf{1}_{B_\rho} X^{-1} K_s g \quad \text{where} \quad M = \mathbf{1}_{B_\rho} X^{-1} K_s (I - \mathbf{1}_{\mathcal{R}_C}) X. \quad (46)$$

We will show below that, under adequate conditions, the linear operator M is a contraction and the sequence (f_n) converges to a function $\mathcal{A}(f)$ when $n \rightarrow \infty$.

6.3 Convergence of convolution-based reconstruction

Before the main theorem on the convergence of the convolution-based reconstruction algorithm, we present auxiliary results.

On the space of rays Ω_ρ , consider the Laplacian operator Δ on the fibers of the tangent space $\Omega_\rho \subset TS^2$. Given any function $g \in \mathcal{L}^2(\Omega_\rho)$, we define in analogy with $\mathcal{L}(\Omega_\rho)$ the Sobolev norm

$$\|g\|_{\mathcal{L}^2(\Omega_\rho)} := \sum_{\beta=0}^2 \int_{S^2} \|1_{\Omega_\rho} \Delta^\beta g_\theta\|_{L^2(T(\theta))} d\theta,$$

and use a similar definition for $f \in \mathcal{L}^2(B_\rho)$ with the Laplacian on \mathbb{R}^3 , that is,

$$\|f\|_{\mathcal{L}^2(B_\rho)} = \sum_{\beta=0}^2 \|1_{B_\rho} \Delta^\beta f\|_{L^2(\mathbb{R}^3)}.$$

We have then

$$\begin{aligned} \|\Delta^\beta K_s g\|_{L^2(\Omega_\rho)}^2 &= \int_{S^2} \|\Delta^\beta (\gamma_s * g_\theta)\|_{L^2(T(\theta))}^2 d\theta \\ &\leq \int_{S^2} \|\Delta^\beta \gamma_s\|_{L^2(T(\theta))}^2 \|g_\theta\|_{L^1(T(\theta))}^2 d\theta \\ &= \frac{1}{s^{4\beta+2}} \|\Delta^\beta \gamma\|_{L^2(T(\theta))}^2 \int_{S^2} \|g_\theta\|_{L^1(T(\theta))}^2 d\theta \\ &\leq \frac{\max_{\theta \in S^2} |\text{spt } g_\theta|}{s^{4\beta+2}} \|\partial^\beta \gamma\|_{L^2(T(\theta))}^2 \|g\|_{L^2(\Omega_\rho)}^2. \end{aligned}$$

As above, we choose a radial convolution kernel as in (41). Fix the ball B_ρ of radius $\rho > 0$ and let $C \subset B_\rho$ be a ball of radius $\eta \rho$, with $0 < \eta < 1$. Fix a non-negative C^∞ radial function $\kappa(|z|)$, of $z \in \mathbb{R}^3$, such that $\kappa(|z|) = 0$ for $|z| \geq 1$ and $\int_{\mathbb{R}^3} \kappa(|z|) dz = 1$. Then κ determines a smooth radial non-negative function γ defined on \mathbb{R}^2 by the integral (44).

Define the constant c_κ by

$$c_\kappa = \max_{0 \leq \beta \leq 2} \|\Delta^\beta \gamma\|_{L^2(T(\theta))}$$

where the right-hand side does not depend on θ because γ is a radial function in \mathbb{R}^3 . From now on we systematically impose $0 < s < \min(1, \rho)$.

The bound obtained for $\|\Delta^\beta K_s g\|_{L^2(\Omega_\rho)}^2$ then implies by summing terms

$$\|K_s g\|_{\mathcal{L}^2(\Omega_\rho)} \leq \frac{3}{s^5} c_\kappa \max_{\theta \in S^2} |\operatorname{spt} g_\theta|^{1/2} \|g\|_{L^2(\Omega_\rho)}. \quad (47)$$

The Fourier transforms of derivatives and Cauchy-Schwarz inequality give the natural bounds

$$\begin{aligned} (1 + |v|)^4 |\mathcal{F}_\theta g_\theta(v)| &\leq (2\pi)^{-4} \sum_{\beta=0}^2 \int_{T(\theta)} |\Delta^\beta g_\theta(u)| du \\ &\leq (2\pi)^{-4} |\operatorname{spt} g_\theta|^{1/2} \sum_{\beta=0}^2 \|\Delta^\beta g_\theta\|_{L^2(B_\rho(\theta))} \\ &\leq \frac{3 |\operatorname{spt} g_\theta|^{1/2}}{(2\pi)^4} \left(\sum_{\beta=0}^2 \|\Delta^\beta g_\theta\|_{L^2(B_\rho(\theta))}^2 \right)^{1/2} \\ &\leq \frac{3 |\operatorname{spt} g_\theta|^{1/2}}{(2\pi)^4} \sum_{\beta=0}^2 \|\Delta^\beta g\|_{L^2(\Omega_\rho)}. \end{aligned}$$

The last inequality, derived from (11) and the Pythagorean inequality, can now be inserted in the inversion formula (15) to yield

$$\|X^{-1}g\|_{L^\infty(\mathbb{R}^3)} \leq \frac{3}{(2\pi)^7} \max_{\theta \in S^2} |\operatorname{spt} g_\theta|^{1/2} \|g\|_{\mathcal{L}^2(\Omega_\rho)} \leq \frac{3}{2^7 \pi^{6.5}} \rho \|g\|_{\mathcal{L}^2(\Omega_\rho)}. \quad (48)$$

For $0 < s < \min(1, \rho)$, let K_s be the family of ray convolution operators determined by κ on the space of rays Ω_ρ , as defined by (40). Let $f \in L^\infty(B_\rho)$ and $g = \mathbf{1}_{\mathcal{R}_C} X f$. The convolution-based ROI reconstruction algorithm defined in (46) by the kernel K_s generates a sequence of functions $(f_n) \in L^2(\mathbb{R}^3)$ by the recursive affine equation

$$f_n = M f_{n-1} + h, \quad (49)$$

where $M = \mathbf{1}_{B_\rho} X^{-1} K_s (I - \mathbf{1}_{\mathcal{R}_C}) X$ and $h = \mathbf{1}_{B_\rho} X^{-1} K_s g$. Define the critical parameter $\nu(\rho, \eta, s)$ by

$$\nu(\rho, \eta, s) = 0.0042 \rho^{7/2} c_\kappa \frac{(1 - \eta^2)^{1/2}}{s^5}.$$

Note that, for fixed κ, ρ and each fixed $s > 0$, the value $\nu(\rho, \eta, s)$ tends to 0 as $\eta < 1$ tends to 1 or, equivalently, when the residual volume $|B_\rho \setminus C|$ around the spherical ROI tends to 0.

Theorem 2. Fix $s > 0$ and $\eta < 1$ such that $\nu(\rho, \eta, s) < 1$. Then, for each $f \in L^\infty(B_\rho)$, the sequence (f_n) defined by (49) converges exponentially fast in $L^2(B_\rho)$ to

$$\mathcal{A}(f) = \lim_{n \rightarrow \infty} f_n$$

and \mathcal{A} is a bounded linear operator on $L^2(B_\rho)$.

Moreover, if one imposes $\nu(\rho, \eta, s) < 0.9$, then, for any $f \in L^\infty(B_\rho)$, the reconstruction error $\mathcal{A}(f) - f$ is bounded by

$$\|\mathcal{A}(f) - f\|_{L^2(\mathbb{R}^3)} \leq 1.005 (1 + \rho)^{3/2} \|\mu_s * f - f\|_{L^2(\mathbb{R}^3)}$$

where $\mu_s *$ is the convolution by the radial function $\frac{1}{s^3} \kappa(\frac{|z|}{s})$, as defined by (41).

For any fixed $f \in L^2(B_\rho)$, since $\lim_{s \rightarrow 0} \|\mu_s * f - f\|_{L^2(\mathbb{R}^3)} = 0$, the reconstruction error $\|\mathcal{A}(f) - f\|_{L^2(\mathbb{R}^3)}$ can hence be as small as desired provided s and $1 - \eta$ are small enough.

Proof. For any $f \in L^\infty(B_\rho)$, the linear operator M verifies

$$\|Mf\|_{L^2(B_\rho)} \leq |B_\rho|^{1/2} \|Mf\|_{L^\infty(B_\rho)}$$

and hence, using the bound (48), we have:

$$\|Mf\|_{L^2(B_\rho)} \leq |B_\rho|^{1/2} \frac{3}{(2\pi)^7} \max_{\theta \in S^2} |B_{\rho+s}(\theta)|^{1/2} \|K_s(I - \mathbf{1}_{\mathcal{R}_C})Xf\|_{\mathcal{L}^2(\Omega_{\rho+s})}.$$

Here $B_{\rho+s}(\theta)$ is the orthogonal projection of the ball $B_{\rho+s}$ on $T(\theta)$, so that $|B_{\rho+s}(\theta)| \leq 4\pi\rho^2$ and the last inequality becomes

$$\|Mf\|_{L^2(B_\rho)} \leq \frac{3}{32\sqrt{3}\pi^6} \rho^{5/2} \|K_s(I - \mathbf{1}_{\mathcal{R}_C})Xf\|_{\mathcal{L}^2(\Omega_\rho)}. \quad (50)$$

Applying (47) and denoting by $C(\theta)$ the orthogonal projection of the ball C on $T(\theta)$, we have

$$\|K_s(I - \mathbf{1}_{\mathcal{R}_C})Xf\|_{\mathcal{L}^2(\Omega_{\rho+s})} \leq \frac{9}{s^5} c_\kappa \max_{\theta \in S^2} |B_\rho(\theta) \setminus C(\theta)|^{1/2} \|Xf\|_{L^2(\mathbb{R}^3)}.$$

By construction, $|B_\rho(\theta) \setminus C(\theta)|$ is at most $\pi\rho^2(1 - \eta^2)$ and the bound (13) yields $\|Xf\|_{L^2(\mathbb{R}^3)} \leq 2\pi\sqrt{2\rho} \|f\|_{L^2(B_\rho)}$, which in turn implies

$$\|K_s(I - \mathbf{1}_{\mathcal{R}_C})Xf\|_{\mathcal{L}^2(\Omega_{\rho+s})} \leq \frac{9}{s^5} c_\kappa \pi^{1/2} \rho (1 - \eta^2)^{1/2} \|f\|_{L^2(\mathbb{R}^3)}.$$

Combining this bound with (50), we obtain

$$\|Mf\|_{L^2(B_\rho)} \leq \frac{81}{32\sqrt{3}\pi^{5.5}} c_\kappa \rho^{7/2} \frac{(1-\eta^2)^{1/2}}{s^5} \|f\|_{L^2(B_\rho)}.$$

Hence the linear operator $M : L^2(B_\rho) \rightarrow L^2(B_\rho)$ has a norm bounded by

$$\|M\|_{L^2(B_\rho)} \leq \nu = \nu(\rho, \eta, s) = 0.0042 c_\kappa \rho^{7/2} \frac{(1-\eta^2)^{1/2}}{s^5}.$$

It follows that whenever $\nu < 1$, then M is a strict contraction of $L^2(B_\rho)$. For each given $s < \min(1, \rho)$, we can always enforce $\nu < 1$, provided η is close enough to 1. This is equivalent to requiring that the volume of our spherical ROI is large enough within the ball B_ρ . From now on, we will consider only pairs (s, η) verifying $\nu(\rho, \eta, s) < 1$.

The ROI truncated data $g = \mathbf{1}_{\mathcal{R}_C} X f$ enable the iterative computation of the approximate density reconstructions $f_{n+1} = Mf_n + h$, where

$$h = \mathbf{1}_{B_\rho} X^{-1} K_s g = \mathbf{1}_{B_\rho} X^{-1} K_s \mathbf{1}_{\mathcal{R}_C} X f. \quad (51)$$

Since M is a strict contraction of $L^2(B_\rho)$, the sequence (f_n) must then converge at exponential speed in $L^2(B_\rho)$ to a limit $\mathcal{A}(f)$, which obviously verifies

$$\mathcal{A}(f) = \sum_{k=0}^{\infty} M^k h \quad \text{and} \quad \mathcal{A}(f) = M\mathcal{A}(f) + h. \quad (52)$$

Inequalities (13), (45), (48) provide bounds for the norms of three linear operators, namely

$$\begin{aligned} \|U\| &\leq 2\pi(2\rho)^{1/2} & \text{where } U = \mathbf{1}_{\mathcal{R}_C} X \text{ maps } L^2(B_\rho) \text{ into } L^2(\Omega_\rho), \\ \|V\| &\leq 1 & \text{where } V = K_s \text{ maps } L^2(\Omega_\rho) \text{ into } L^2(\Omega_{\rho+s}), \\ \|W\| &\leq \frac{3}{2\pi^{6.5}}(1+\rho) & \text{where } W = \mathbf{1}_{B_\rho} X^{-1} \text{ maps } L^2(\Omega_{\rho+s}) \text{ into } L^2(B_\rho). \end{aligned}$$

Rewriting equation (51) as $h = WVUf$ then yields

$$\|h\|_{L^2(B_\rho)} \leq \|W\| \|V\| \|U\| \|f\|_{L^2(B_\rho)} \leq \frac{3}{(2\pi)^{5.5}} \rho^{1/2} (1+\rho) \|f\|_{L^2(B_\rho)}.$$

The series (52) entails $\|\mathcal{A}(f)\|_{L^2(B_\rho)} \leq \frac{1}{1-\nu} \|h\|_{L^2(B_\rho)}$ and hence \mathcal{A} verifies, for all f in $L^2(B_\rho)$,

$$\|\mathcal{A}(f)\|_{L^2(B_\rho)} \leq \frac{1}{1-\nu(\rho, \eta, s)} \frac{3}{(2\pi)^{5.5}} \rho^{1/2} (1+\rho) \|f\|_{L^2(B_\rho)}. \quad (53)$$

To study the reconstruction error $\|\mathcal{A}(f) - f\|_{L^2(B_\rho)}$, we first consider the case where f is in $\mathcal{L}^2(B_\rho)$. Note that, by (51), the function h verifies the two identities

$$\mathbf{1}_{B_\rho} X^{-1} K_s X f = Mf + h \quad \text{and} \quad \mathcal{A}(f) = M\mathcal{A}(f) + h$$

and they immediately yield the identity

$$\mathcal{A}(f) - f = M(\mathcal{A}(f) - f) + \mathbf{1}_{B_\rho} X^{-1} K_s X f - f.$$

This implies the inequality

$$\|\mathcal{A}(f) - f\|_{L^2(\mathbb{R}^3)} \leq \nu \|\mathcal{A}(f) - f\|_{L^2(\mathbb{R}^3)} + \|\mathbf{1}_{B_\rho} X^{-1} K_s X f - f\|_{L^2(\mathbb{R}^3)}.$$

For $f \in \mathcal{L}^2(B_\rho)$ we have that $f = \mathbf{1}_{B_\rho} X^{-1} X f$ and $(K_s - I)Xf$ has its support in $\Omega_{\rho+s} \subset \Omega_{2\rho}$. Combining this observation with the preceding inequality, we get

$$(1 - \nu) \|\mathcal{A}(f) - f\|_{L^2(\mathbb{R}^3)} \leq \|\mathbf{1}_{B_\rho} X^{-1} (K_s - I)Xf\|_{L^2(\mathbb{R}^3)}.$$

The bound (48) on $\|X^{-1}\|$ then implies

$$\|\mathcal{A}(f) - f\|_{L^2(\mathbb{R}^3)} \leq \frac{1}{1 - \nu} \frac{3}{2^6 \pi^{6.5}} \rho \|(K_s - I)Xf\|_{\mathcal{L}^2(\Omega_{\rho+s})}. \quad (54)$$

The commutation relation (42) entails $(K_s - I)Xf = X(\mu_s * f - f)$ and, hence, in view of (13),

$$\|(K_s - I)Xf\|_{\mathcal{L}^2(\Omega_{\rho+s})} = \|X(\mu_s * f - f)\|_{\mathcal{L}^2(\Omega_{\rho+s})} \leq 4\pi\sqrt{\rho} \|\mu_s * f - f\|_{L^2(\mathbb{R}^3)}.$$

Inserting this bound into equation (54) then provides the following estimate for the reconstruction error valid for all $f \in \mathcal{L}^2(B_\rho)$:

$$\|\mathcal{A}(f) - f\|_{L^2(\mathbb{R}^3)} \leq \frac{3}{16\pi^{5.5}} \frac{\rho^{3/2}}{1 - \nu(\rho, \eta, s)} \|\mu_s * f - f\|_{L^2(\mathbb{R}^3)}. \quad (55)$$

Consider now the generic case where f is only assumed to be in $L^2(B_\rho)$. The function $F = \mu_s * f$ is then in $\mathcal{L}^2(B_{\rho+s})$ and, hence, in $\mathcal{L}^2(B_{\rho+1})$. On this last space, we want the operator \mathcal{A} to be well defined, so we will require that

$$\nu(1 + \rho, \eta, s) = 0.0042 c_\kappa (1 + \rho)^4 \frac{(1 - \eta^2)^{1/2}}{s^5} \leq 0.9.$$

This implies that $1/(1 - \nu(1 + \rho, \eta, s)) \leq 10$.

Let us introduce the temporary abbreviated notation $H = L^2(\mathbb{R}^3)$. The error bound (55) applied to the function $F \in \mathcal{L}^2(B_{\rho+1})$ yields

$$\|\mathcal{A}(F) - F\|_H \leq \frac{9}{8\pi^{5.5}} (1 + \rho)^{3/2} \|\mu_s * F - F\|_H. \quad (56)$$

Since $F = \mu_s * f$ and since μ_s is a positive measure of mass 1 on \mathbb{R}^3 we have

$$\|\mu_s * F - F\|_H = \|\mu_s * (\mu_s * f - f)\|_H \leq \|\mu_s * f - f\|_H.$$

Hence inequality (56) entails a fortiori

$$\|\mathcal{A}(F) - F\|_H \leq \frac{9}{8\pi^{5.5}} (1 + \rho)^{3/2} \|\mu_s * f - f\|_H.$$

The triangle inequality in the Hilbert space H then yields

$$\|\mathcal{A}(f) - f\|_H \leq \|\mathcal{A}(f) - \mathcal{A}(F)\|_H + \|\mathcal{A}(F) - F\|_H + \|F - f\|_H.$$

But $F - f \in L^2(B_{\rho+1})$ implies $\|\mathcal{A}(f) - \mathcal{A}(F)\|_H = \|\mathcal{A}(F - f)\|_{L^2(B_{\rho+1})}$ and, hence, inequality (53) provides the bound

$$\|\mathcal{A}(f) - \mathcal{A}(F)\|_H \leq \frac{9}{8\sqrt{2}\pi^{5.5}} (1 + \rho)^{3/2} \|F - f\|_H.$$

Combining the last three inequalities then directly provides the bound

$$\|\mathcal{A}(f) - f\|_H \leq \left(1 + \frac{9}{4\pi^{5.5}}\right) (1 + \rho)^{3/2} \|F - f\|_H$$

and, hence, a fortiori the announced bound valid for all $f \in L^2(B_\rho)$

$$\|\mathcal{A}(f) - f\|_{L^2(\mathbb{R}^3)} \leq 1.005 (1 + \rho)^{3/2} \|\mu_s * f - f\|_{L^2(\mathbb{R}^3)}. \quad \square$$

7 Conclusion and future work

In this paper, we have presented a thorough mathematical study of two types of iterative ROI reconstruction algorithms valid the continuous setting of X-ray data generated by a dense set of sources located on a sphere surrounding the object, but restricted to the rays intersecting a fixed spherical ROI. We

have established their convergence properties and evaluated the reconstruction errors. In particular, our convolution based ROI reconstruction method regularizes X-ray data at each iterative step by a natural *linear convolution kernel* on the space of rays. This enables a very precise mathematical analysis of ROI reconstruction convergence in L^2 -norm, with controlled bounds on the L^2 -error of reconstruction. This result offers a mathematical advantage with respect to our wavelet-based ROI reconstruction algorithm where, at each iterative step, wavelet regularization is *non linear* and generates approximate current densities by expansion on a large but *finite wavelet basis*.

Together with our theoretical analysis, we have presented a numerical study of our ROI reconstruction algorithm in the case of wavelet-based ROI regularization using simulated acquisition. For this numerical study, we have considered three classical discrete acquisition schemes for CT, including the cases of sources distributed on a circle and an helix. Our discrete simulation results confirm the existence of a critical ROI radius for which our wavelet-based ROI reconstruction algorithm converges at exponential speed to a good quality reconstruction, as predicted by the theoretical analysis. In fact, numerical results show that such critical radius is fairly small.

Practical know-how for iterative ROI reconstruction tends to favor direct regularizations of the current X-ray data at each step, so we intend in future work to explore the concrete performances of our convolution based ROI reconstruction. We will also extend the theoretical analysis presented here to ROI truncated X-ray data generated by a sources located on a curve, as this is more consistent with practical CT setups.

Acknowledgements

The authors thank M. Motamedi and I. Patrikeev, at the Center of Biomedical Engineering, University of Texas Medical Branch, for providing the micro-CT images in Figures 6-8. A.S. and R.A. acknowledge support by a Methodist Hospital grant provided by Dr. K. Li, MD, Chair of Radiology. B.G.B. is grateful for partial support by NSF DMS 1109545 and by the Alexander von Humboldt foundation, and for the great hospitality in Gitta Kutyniok's group at the Technische Universität Berlin, where part of this work was completed. D.L. acknowledges partial support by NSF DMS 1005799 and DMS 1008900.

References

- [1] C. I. Lee, A. H. Haims, and E. P. Monico et al., “Diagnostic ct scans: assessment of patient, physician, and radiologist awareness of radiation dose and possible risks,” *Radiology*, vol. 231, no. 2, pp. 393–398, 2004.
- [2] W. Huda, W. Randazzo, and S. Tipnis et al., “Embryo dose estimates in body ct,” *AJR Am J Roentgenol*, vol. 194, no. 4, pp. 874–880, 2010.
- [3] F. Natterer and F. Wubbeling, *Mathematical Methods in Image Reconstruction*. SIAM: Society for Industrial and Applied Mathematics, 2001.
- [4] F. Natterer, *The Mathematics of Computerized Tomography*. SIAM: Society for Industrial and Applied Mathematics, 2001.
- [5] R. Clackdoyle and M. Defrise, “Tomographic reconstruction in the 21st century. region-of-interest reconstruction from incomplete data,” *IEEE Signal Processing*, vol. 60, pp. 60–80, 2010.
- [6] G. Wang and H. Yu, “The meaning of interior tomography,” *Physics in Medicine and Biology*, vol. 58, no. 16, p. R161, 2013. [Online]. Available: <http://stacks.iop.org/0031-9155/58/i=16/a=R161>
- [7] F. Noo, M. Defrise, R. Clackdoyle, and H. Kudo, “Image reconstruction from fan-beam projections on less than a short scan,” *Physics in Medicine and Biology*, vol. 47, no. 14, pp. 2525–2546, 2002.
- [8] R. Clackdoyle and F. Noo, “A large class of inversion formulae for the 2-d radon transform of functions of compact support,” *Inverse Problems*, vol. 20, pp. 1281–1291, 2004.
- [9] Y. Zou, X. Pan, and E. Sidky, “Image reconstruction in regions-of-interest from truncated projections in a reduced fan-beam scan,” *Phys. Med. Biol.*, vol. 50, pp. 13–28, 2005.
- [10] G. T. Herman and R. Davidi, “Image reconstruction from a small number of projections,” *Inverse Problems*, vol. 24, no. 4, 2008.
- [11] E. Sidky, C. Kao, and X. Pan, “Accurate image reconstruction from few views and limited angle data in divergent beam CT,” *Medical Physics*, vol. 1, 2009.

- [12] G. Yan, J. Tian, S. Zhu, C. Qin, Y. Dai, F. Yang, D. Dong, and P. Wu, “Fast Katsevich algorithm based on GPU for helical cone-beam computed tomography,” *Information Technology in Biomedicine, IEEE Transactions on*, vol. 14, no. 4, pp. 1053–1061, 2010.
- [13] H. Yu and G. Wang, “Compressed sensing based interior tomography,” *Physics in Medicine and Biology*, vol. 54, no. 9, pp. 2791–2805, 2009. [Online]. Available: <http://dx.doi.org/10.1088/0031-9155/54/9/014>
- [14] M. Nassi, W. R. Brody, B. P. Medoff, and A. Macovski, “Iterative reconstruction-reprojection: An algorithm for limited data cardiac-computed tomography,” *Biomedical Engineering, IEEE Transactions on*, vol. BME-29, no. 5, pp. 333–341, 1982.
- [15] J. Kim, K. Y. Kwak, S.-B. Park, and Z. H. Cho, “Projection space iteration reconstruction-reprojection,” *Medical Imaging, IEEE Transactions on*, vol. 4, no. 3, pp. 139–143, 1985.
- [16] A. Ziegler, T. Nielsen, and M. Grass, “Iterative reconstruction of a region of interest for transmission tomography,” *Medical Physics*, vol. 35, no. 4, pp. 1317–1327, 2008.
- [17] A. Katsevich, “An improved exact filtered backprojection algorithm for spiral computed tomography,” *Advances in Applied Mathematics*, vol. 32, pp. 681–697, 2004.
- [18] H. Yu and G. Wang, “Studies on implementation of the Katsevich algorithm for spiral cone-beam CT,” *Journal of X-Ray Science and Technology*, vol. 12, pp. 97–116, 2004.
- [19] H. Tuy, “An inversion formula for cone-beam reconstruction,” *SIAM Journal on Applied Mathematics*, vol. 43, no. 3, pp. 546–552, 1983.
- [20] S. Zhao, H. Yu, and G. Wang, “A unified framework for exact cone-beam reconstruction formulas.” *Medical physics*, vol. 32, no. 6, pp. 1712–1721, Jun. 2005.
- [21] S. Mallat, *A Wavelet Tour of Signal Processing, Third Edition: The Sparse Way*, 3rd ed. Academic Press, 2008.

- [22] D. L. Donoho, “Nonlinear solution of linear inverse problems by wavelet-vaguelette decomposition,” *Applied and Computational Harmonic Analysis*, vol. 2, pp. 101–126, 1995.
- [23] G. Steidl, J. Weickert, T. Brox, P. Mrazek, and M. Welk, “On the equivalence of soft wavelet shrinkage, total variation diffusion, total variation regularization, and sides,” *SIAM Journal on Numerical Analysis*, vol. 42, no. 2, pp. 686–713, 2004.
- [24] B. Dong, J. Li, and Z. Shen, “X-ray CT image reconstruction via wavelet frame based regularization and Radon domain inpainting,” *J. Sci. Comput.*, vol. 54, no. 2-3, pp. 333–349, Feb. 2013.